The Split-cavity Cross-coupled Extrinsic Fiber Interferometer

by

Rajat R. Dhawan

Thesis submitted to the Faculty of the
Virginia Polytechnic Institute and State University
in partial fulfillment of the requirements for the degree of
MASTER OF SCIENCE

in

Electrical Engineering

APPROVED:

Richard O. Claus

Dr. Richard O. Claus, Chairman

Kent A. Murphy

Dr. Kent A. Murphy

Dr. Ira Jacobs

August 1994
Blacksburg, Virginia

The Split-cavity Cross-coupled Extrinsic Fiber Interferometer

by

Rajat R. Dhawan

Richard O. Claus, Chairman

Electrical Engineering

(ABSTRACT)

Fiber optic interferometric sensors have been used to measure a number of physical measurands like strain and temperature. Among the different interferometric sensor configurations in use today, the Fabry-Perot interferometer has been shown to have a high sensitivity. The extrinsic Fabry-Perot sensor (EFPI) is a very good candidate for smart structure applications. In this thesis, a new configuration of the extrinsic Fabry-Perot interferometer is developed and demonstrated. This new configuration, based on four-beam interference, utilizes two EFPI sensor heads on a single directional coupler in a Split-cavity Cross-coupled Extrinsic Fiber Interferometer (SCEFI) arrangement. This sensor configuration eliminates the need for biasing the phase difference at the quadrature point. The spectrum analysis scheme, devised for signal demodulation of the SCEFI output allows a linear readout of the phase shift. Both dynamic and static phase shifts are considered. The spectrum analysis scheme developed in this thesis, also allows independent measurements of the phase shift in the two sensor heads. This leads to the multiplexing of two sensors, using a single source and a single coupler. The application of the SCEFI to two-sensor multiplexing is demonstrated experimentally in this thesis. Other significant applications of this new sensor configuration are also discussed.

Acknowledgments

I would like to thank my committee chairman Dr. Richard O. Claus for giving me the opportunity to work at the Fiber and Electro-optics Research Center and for his support throughout my graduate program. His constant encouragement, co-operation, and positive comments has made my graduate education a rewarding experience. I would also like to thank Dr. Jacobs and Dr. Murphy for serving on my committee and for their extremely useful comments on this thesis.

I acknowledge and thank Dr. V. S. Sudarshanam for his guidance through every step of this research. I would also like to thank Mike Gunther for his support throughout my stay at FEORC.

I thank the students and staff of FEORC for making it a wonderful place to pursue graduate studies. A number of my friends have helped me along the way and I thank Anjana, Asif, Mallika, Nirmal, Ravi, Shankar, Sridhar and Veeru for their support. A special thanks to Vivek Arya for helping me with the presentation aspect of this thesis.

Finally, I acknowledge the support of my parents, Rajinder and Rajesh Dhawan and my grandfathers, Kundan Lal Dhawan and the late H. C. Dass. They have been a tremendous source of inspiration for me and I shall always strive to follow their path in life. A very special thanks to my sister, Ramona Mehta, for being my closest friend and all the fond memories of our childhood.

Table of Contents

Title page i

Abstract ii

Acknowledgments iii

Table of Contents iv

List of Figures vii

Chapter 1 - Introduction 1

1.1 Optical fiber sensors 1

1.2 Intensity sensors 2

1.3 Interferometric sensors 4

1.3.1 Mach-Zehnder interferometer 6

1.3.2 Michelson interferometer 8

1.3.3 Fabry-Perot interferometer 8

Chapter 2 - Extrinsic Fabry-Perot Interferometer 11

2.1 Introduction 11

2.2 Theory and fabrication 12

2.3 Advantages of the EFPI 18

2.4 Limitations of the EFPI 18

Chapter 3 - Detection Schemes for Fiber Interferometers 22

3.1 Basic operation of fiber interferometers 22

3.2 Signal processing techniques 23

3.2.1 Active homodyne 24
3.2.1.1 Advantages and limitations of the active homodyne technique 29
3.2.2 Passive homodyne technique 30
3.2.3 Heterodyne detection 32
3.3 Spectrum analysis methods of optical phase detection 34

Chapter 4 - The Split-cavity Cross-coupled Extrinsic Fiber Interferometer 39
4.1 Introduction 39
4.2 Optical configuration of SCEFI 42
4.3 Theory and signal detection 44
4.3.1 New spectrum analysis scheme for the SCEFI 45

Chapter 5 - Experimental Configuration, Results and Discussion 53
5.1 Experimental arrangement 53
5.2 Results and discussion 57

Chapter 6 - Applications to two-sensor multiplexing 73
6.1 Introduction 73
6.2 Spectrum analysis detection method for multiplexing 74
6.3 Experimental arrangement 77
6.4 Results and discussion 80

Chapter 7 - Conclusions and Future Directions 85
7.1 Conclusions 85
7.2 Future directions 86

References 88

Vita 92

List of Figures

Figure 1.1 An intensity-based fiber optic sensor 3

Figure 1.2 Fiber optic Mach-Zehnder interferometer..... 7

Figure 1.3 Fiber optic Michelson interferometer..... 9

Figure 1.4 Intrinsic fiber optic Fabry-Perot interferometer..... 10

Figure 2.1 Extrinsic Fabry-Perot Interferometer with details of the sensor system ... 14

Figure 2.2 Variation of the output intensity of the EFPI for increasing air-gap separation..... 17

Figure 2.3 Signal fading in fiber interferometers..... 20

Figure 3.1 Active homodyne demodulation technique.
Output A: low-gain approach Output B: high-gain approach..... 28

Figure 3.2 Passive demodulation technique utilizing two signals 90° out of phase ... 31

Figure 4.1 Schematic of the Split-cavity Cross-coupled Extrinsic Fiber Interferometer..... 43

Figure 5.1 Experimental arrangement of the SCEFI 55

Figure 5.2a SCEFI detection using an additional coupler..... 56

Figure 5.2b Two-detector support system for the SCEFI..... 56

Figure 5.3a FFT of the SCEFI output at D4 (lower trace) and D3 (upper trace) at an arbitrary sampling instant. 60

Figure 5.3b FFT of the SCEFI output at D4 (lower trace) and D3 (upper trace) at a different sampling instant..... 61

Figure 5.4a FFT of the SCEFI output at D2 for a difference frequency of 500 Hz..... 62

Figure 5.4b FFT of the SCEFI output at D2 for a difference frequency of 500 Hz,

at a different sampling instant. 63

Figure 5.5a FFT of the output of a single EFPI at the sensor head (upper traces, at D1) and the SCEFI (lower traces, at D2), for a signal applied to the sensor head alone. 64

Figure 5.5b FFT of the output of a single EFPI at the sensor head (upper traces, at D1) and the SCEFI (lower traces, at D2), for a signal applied to the sensor head alone, for a different sampling instant. 65

Figure 5.5c FFT of the output of a single EFPI at the sensor head (upper traces, at D1) and the SCEFI (lower traces, at D2), for a signal applied to both the sensor head and the modulator head. 66

Figure 5.6a FFT of the SCEFI output at D4 for a signal at 2.99 kHz and modulator at 3.69 kHz 67

Figure 5.6b FFT of the SCEFI output at D4 for a signal at 2.99 kHz and modulator at 3.69 kHz, for a different sampling instant 68

Figure 5.7a Time domain plot of the SCEFI output at D4 for an injection current of 28.2 mA. 69

Figure 5.7b Frequency domain plot of the SCEFI output at D4 for an injection current of 28.2 mA 70

Figure 5.8a FFT of the SCEFI output at D4 for an injection current of 29.8 mA 71

Figure 5.8b FFT of the SCEFI output at D4 for an injection current of 30.1 mA 72

Figure 6.1a Schematic of the SCEFI 78

Figure 6.1b Test modulator arrangement for each sensor head 78

Figure 6.2 Optical spectrum of the laser diode output. a) several modes, b) single strong mode 79

Figure 6.3 FFT of the detector output for an input of 45V at 1.4kHz to EFPI 1, with no drive to EFPI 2 81

Figure 6.4 FFT of the SCEFI output for an input voltage of 25V to each of the two EFPI's..... 82

Figure 6.5 Frequency domain and time domain outputs for the SCEFI for an input voltage of 34V to both the EFPI's..... 83

Figure 6.6 Phase shift measured by the $J_1.J_3$ method as a function of input voltage to the PZT test modulators..... 84

Chapter 1. Introduction

1.1 Optical fiber sensors

The use of optical fibers in the telecommunication industry has led to rapid advances in the field of communication systems. The improvements in the related areas of optoelectronics and optical signal processing has led to the growing interest in fiber optic sensors. Fiber optic sensors offer a number of advantages over conventional sensors [1].

- Passive (all dielectric)
- Light weight
- Small size
- Increased sensitivity over existing techniques
- Immunity to EMI
- High temperature performance
- Large bandwidth
- Environmental ruggedness to vibration and shock
- Multiplexing capabilities
- Can be used in high voltage, electrically noisy or other stressing environments

The above mentioned advantages have led to the use of optical fibers as sensors in a wide variety of applications to measure parameters like strain, temperature, pressure, liquid-level, acceleration, voltage, and current [1].

Optical fiber sensors can be broadly classified into interferometric (or phase) sensors and intensity sensors [2].

1.2 Intensity sensors

Intensity sensors are inherently simple and require only a modest amount of support electronics. The advantages of intensity sensors are the simplicity of construction and their compatibility with multimode fiber technology. However, in such sensors, sensitivity is traded off to realize these advantages. An example of an intensity-based fiber optic sensor is shown in Figure 1.1.

In this example, light travels along a multi mode fiber, and strikes a movable reflector. Light is reflected from the mirror and it reenters the fiber. The amount of light reflected back into the fiber, is determined by the position of the reflector. As the reflector is moved away from the fiber, less light is coupled back into the fiber.

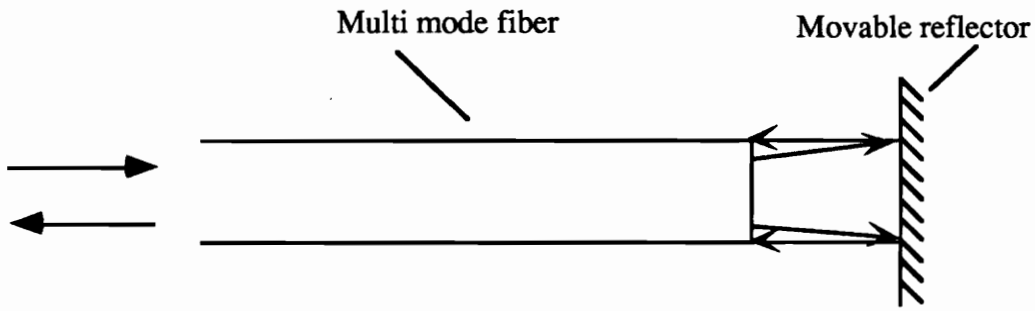

Figure 1.1 An intensity-based fiber optic sensor [2]

However, such sensors, though simple, are handicapped by the lack of a suitable reference signal, and also by light source fluctuations, fiber losses and variations in modal power distribution (MPD) in fibers. All these factors cause changes in the output of the sensor which may be misinterpreted as changes in the value of the measurand. Recently, Wang et al., have proposed a Split-Spectrum Intensity-Based (SSIB) strain sensor approach [3] which compensates for both fiber loss and source fluctuations.

Other types of intensity sensors, which have been used to sense parameters like strain and pressure, are microbend sensors. These sensors involve bending the fiber to induce radiation losses.

1.3 Interferometric sensors

As opposed to intensity-type sensors, wherein the fiber is used simply to carry the light to the remote optical sensor at the end of the fiber, the fiber plays a more important role in the sensing mechanism of interferometric sensors. The optical losses involved in intensity-based sensors are high as the light has to leave the optical fiber in order to interact with the optical sensor. In interferometric-based sensors, light is not required to exit the fiber in order to interact with the field to be detected. In this type of sensor, the parameter to be detected modulates the phase of the light passing through the fiber. This phase modulation can then be detected by comparing the phase of the light in the signal fiber to that in a reference fiber.

Interferometric sensors have a number of advantages over intensity-based sensors. Firstly, as light is generally confined to the fiber, the sensor has low optical losses. Also, these devices are very sensitive as they are based on the interference of light. They can be used

to measure a number of parameters like strain, temperature, acoustic waves, current and voltage. These sensors also lend themselves to multiplexing possibilities.

A primary drawback of interferometric sensors is that they require relatively complicated signal processing techniques to accomplish effective signal recovery.

The interference of two beams allows the measurement of extremely small differential phase shifts in the optical fiber generated by the measurand. The optical phase shift (in radians) of light passing through a fiber is given by [2],

$$\phi = nkL \tag{1.1}$$

where n is the refractive index of the fiber core, k is the wavenumber in vacuum and L is the physical length of the fiber. The quantity, nL, is defined as the optical path length. The quantity, nk, is denoted by β and is the phase constant of the mode. Small variations in the phase delay can be found by differentiation of equation 1.1.

Thus,

$$\frac{d\phi}{\phi} = \frac{dL}{L} + \frac{dn}{n} + \frac{dk}{k} \tag{1.2}$$

The perturbation to be measured causes physical changes in the fiber and these changes can be described by the first two terms in equation 1.2. Thus, these two terms describe the mechanism by which fibers act as sensors.

In general, the variation in the phase delay due to changes in pressure, magnetic field and temperature is due to the dL and dn terms. The change in the refractive index of the core is due to the strain optic coefficient of the fiber. The last term takes into account any wavelength variation associated with the source. The dL term is the dominant term in equation 1.2 and is caused by the bonding of some type of material to the fiber.

Some of the different configurations of the fiber optic interferometer in use today are :

- Mach-Zehnder interferometer
- Michelson interferometer
- Fabry-Perot interferometer

1.3.1 Mach-Zehnder interferometer

Light from the source is split into two beams by a fiber optic coupler. Part of the light is transmitted through the sensing fiber and the remaining part of the light is transmitted through the reference arm. The two outputs are then recombined using another coupler and are allowed to interact on the surface of the photodetector. A suitable demodulator is employed to detect the original phase modulated signal. In this type of an interferometer, the optical phase shift of interest is generated by the sensing arm and the reference arm serves only as a reference path. Such an interferometer is shown in Figure 1.2.

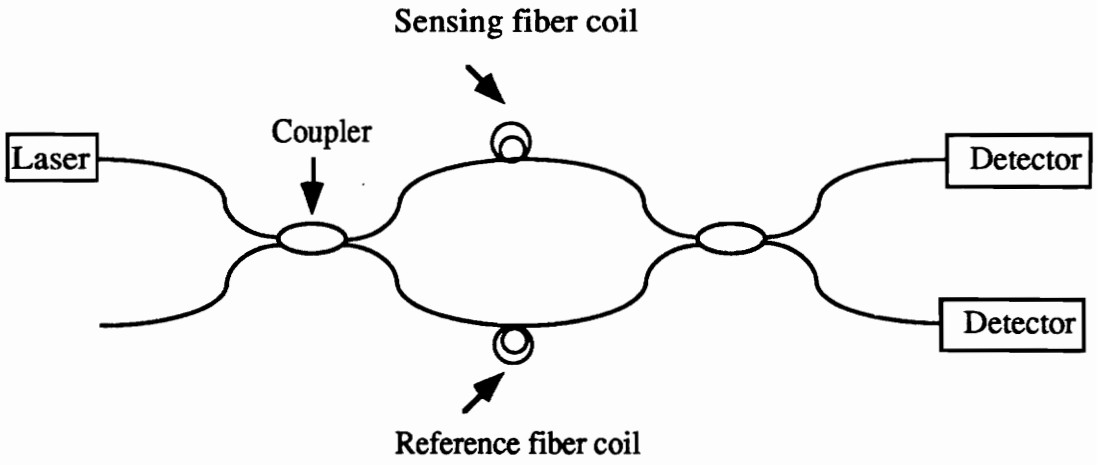

Figure 1.2 Fiber optic Mach-Zehnder interferometer [2]

1.3.2 Michelson interferometer

The configuration of the Michelson interferometer is shown in Figure 1.3. In this kind of an interferometer, there is a single fiber optic coupler that both splits and recombines the light. The light from the source is split by the coupler into the reference and the sensing arms. After traversing the length of the arms, the light is then reflected back through the same arms by the mirrors at the ends of the arms. The light beams, reflected from the mirrors, is then recombined by the coupler. In this sort of an interferometer, the light passes through both the sensing and reference fibers twice. Thus, the optical phase shift per unit length is doubled.

1.3.3 Fabry-Perot interferometer

The Fabry-Perot interferometer is an example of a multiple-beam interferometer. The light from the laser is launched into a fiber. The fiber has two reflective surfaces at its ends. Due to the high reflectivity of the mirrors, the light bounces back and forth within the cavity thus experiencing phase delay in the cavity many times. The multiple reflections that take place between the two mirrors result in an increase in the value of the sensitivity of the sensor. The above Fabry-Perot interferometer version is an example of an intrinsic sensor i.e. the light reflections take place within the cavity enclosed by the mirrors. Another version of the Fabry-Perot interferometer is the extrinsic version wherein the cavity is external to the fiber. Such a sensor is called the Extrinsic Fabry-Perot Interferometer (EFPI) and is the sensor on which this thesis is based.

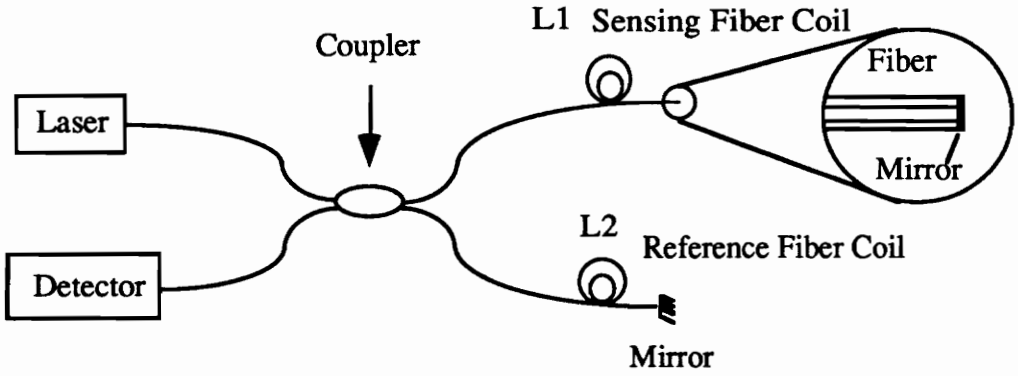

Figure 1.3 Fiber optic Michelson interferometer [2]

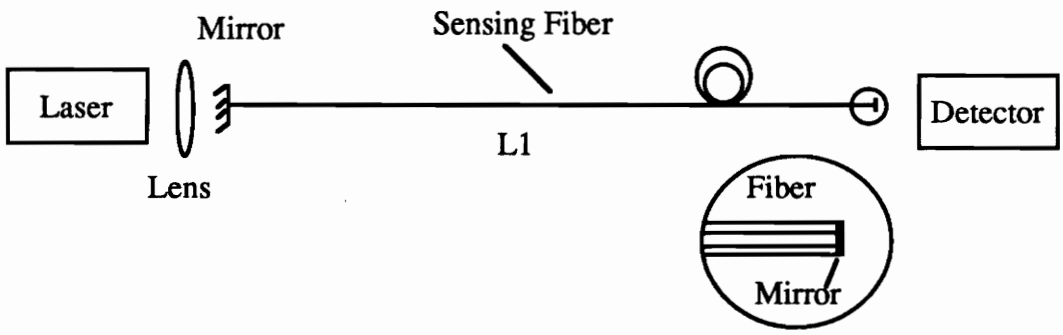

Figure 1.4 Intrinsic fiber optic Fabry-Perot interferometer [2]

Chapter 2. Extrinsic Fabry-Perot Interferometer

2.1 Introduction

The all fiber interferometer has been proven to be very sensitive to external perturbations. This sensitivity of the fiber interferometer has been successfully utilized in the measurement of extremely small phase shifts in the micro-radian range [4].

Optical interferometers are devices that operate on the principle of interference between two or more light beams. This interference phenomenon can be classified as constructive or destructive interference. Constructive interference can be characterized by a maximum signal while destructive interference can be characterized by a minimum signal. In order to have constructive interference, the optical path length difference must be an even multiple of the wavelength while to have destructive interference, the path length difference must be an odd multiple of half wavelength. A fiber optic interferometer has two arms. If the optical path length in one of the arms is varied, a modulation of the phase difference between the two arms results in the measurement of external perturbations.

Fabry-Perot type interferometers depend on the interference of light waves which are reflected from two reflecting surfaces that are in line with the fiber. The two reflecting surfaces enclose a cavity called the Fabry-Perot cavity. Multiple reflections take place inside this cavity. Since the sensor has low reflectivities, only the first reflections are significant. The effect of the subsequent reflections are negligible. The use of such sensors for the detection and measurement of temperature, mechanical vibration and acoustic waves has already been reported [5].

There are two configurations of the fiber optic Fabry-Perot interferometric sensor, intrinsic and extrinsic. Intrinsic sensors are characterized by the confinement of light within the fiber i.e. light is not allowed to leave the fiber. The fabrication of intrinsic sensors involve partial reflective surfaces in line with the fiber. These surfaces could be reflective splices or dielectric mirrors. The extrinsic configuration allows light to exit the fiber. The interference pattern is produced by the reference reflection from the glass-air interface and the sensing reflection from a reflecting surface away from the fiber. The sensor configuration thus consists of an air gap, the Fabry-Perot cavity, which constitutes the sensing region.

2.2 Theory and fabrication

The construction of the Extrinsic Fabry-Perot Interferometer (EFPI), first described by Murphy et al. [6], is shown in Figure 2.1. The sensor comprises an air gap formed by a single mode fiber and a multimode fiber placed inside a hollow core fiber. The single mode fiber is used as the input-output fiber, whereas the multimode fiber is used solely as a reflector. The hollow core fiber is used for aligning the two fibers. The other end of the

multimode fiber is shattered and index-matching gel is used to prevents reflections from this end.

In construction, the multimode fiber is inserted from one end of the hollow core fiber. This fiber is then fused with the hollow core fiber using an arc fusion splice. Next, the single mode fiber is inserted from the other end of the hollow core fiber, to form the air cavity with the fused multimode-hollow core fiber.

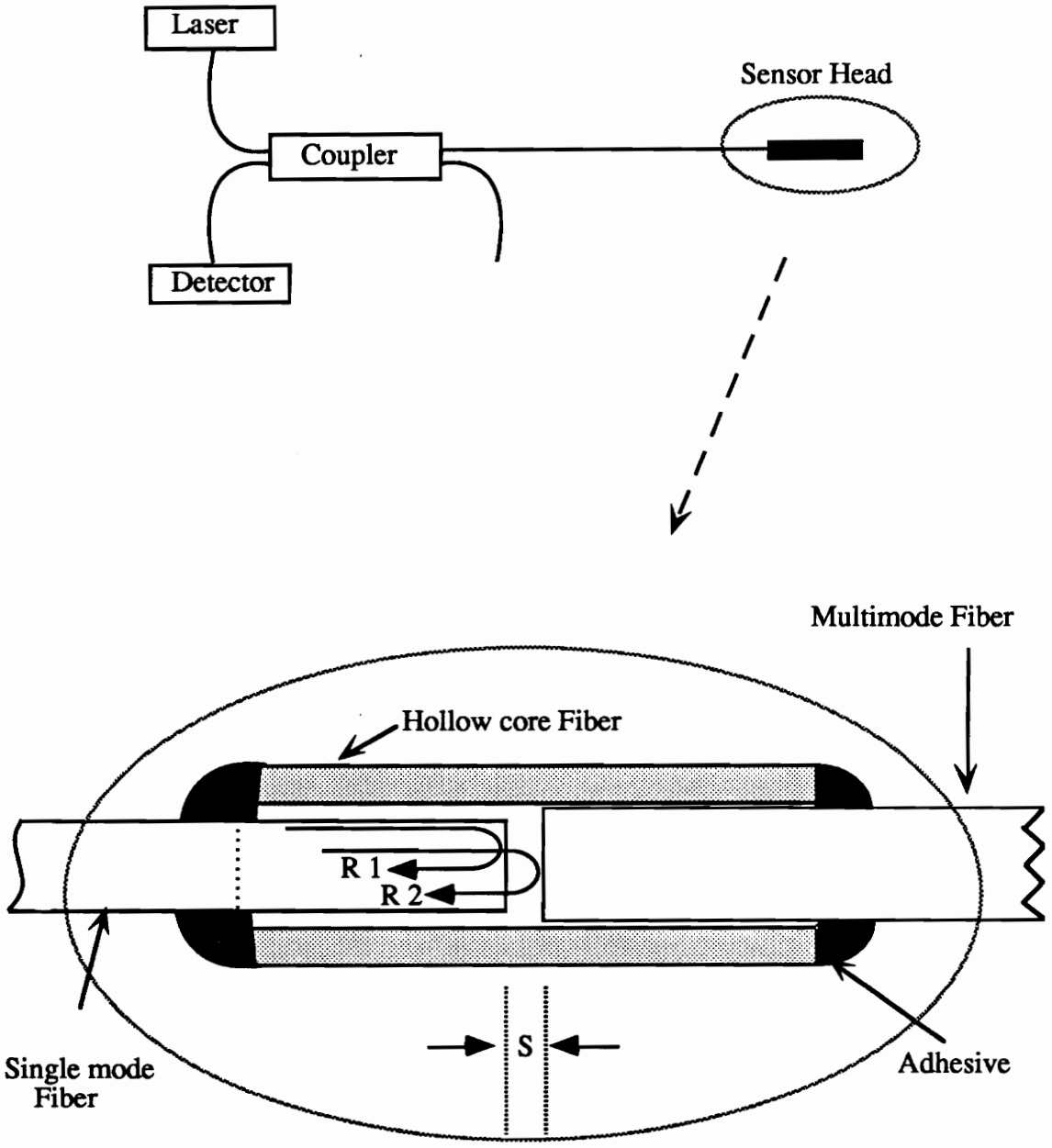

Figure 2.1 Extrinsic Fabry-Perot Interferometer with details of the sensor system [6]

The first reflection is at the glass-air interface. This Fresnel reflection at the front end of the air gap acts as the reference reflection. The second reflection is from the air-glass interface at the far end of the air gap. This constitutes the sensing reflection. These two reflections then interfere in the input-output fiber. As stated above, the effect of subsequent reflections are negligible [7].

The plane wave approximation of the detected output of the EFPI sensor [6], can be represented in terms of its complex amplitude U_i (x, z, t) , and is given by,

$$U_i\,(x,\ z,\ t)\ =\ A_i \exp(\,j\,\phi_i),\quad i=1,2 \tag{2.1}$$

In equation 2.1, A_i is a function of the transverse coordinate, x and the distance traveled, z. The reference and sensing reflections are denoted by the subscripts i=1, 2, respectively. If the reference reflection coefficient, A_1 is denoted by A, then the sensing reflection coefficient is [6],

$$A_2 = A\left\{\frac{t\,a}{a\ +\ 2s\tan\left(\sin^{-1}(NA)\right)}\right\} \tag{2.2}$$

where a is the radius of the core of the fiber, t is the transmission coefficient of the air-glass interface, s is the end separation, and NA is the numerical aperture of the single mode fiber which is given by $NA = \sqrt{n_1^2 - n_2^2}$, where n_1 and n_2 are the refractive indices of the core and cladding, respectively. The output of the sensor is observed as an intensity modulation at the output of the detector which is given by the magnitude squared of the sum of the two amplitudes.

$$I_{det} = |U_1 + U_2|^2 = A_1^2 + A_2^2 + 2A_1A_2\cos(\phi_1 - \phi_2) \quad (2.3)$$

Using equations 2.2 and 2.3, we have [6],

$$I_{det} = A^2\left\{1 + \frac{2ta}{a + 2s\tan\left(\sin^{-1}(NA)\right)}\cos\left(\frac{4\pi s}{\lambda}\right) + \left(\frac{ta}{a + 2s\tan\left(\sin^{-1}(NA)\right)}\right)^2\right\} \quad (2.4)$$

Figure 2.2 shows the variation of the output intensity with increasing gap separation. This intensity drop as the air gap increases can be explained from equation 2.2 which is a simplified loss relation for the longitudinal misalignment of two fibers. As the air gap is increased, the relative intensity of the sensing reflection reduces with respect to the reference reflection. This results in a decrease in the output intensity as the air gap is increased.

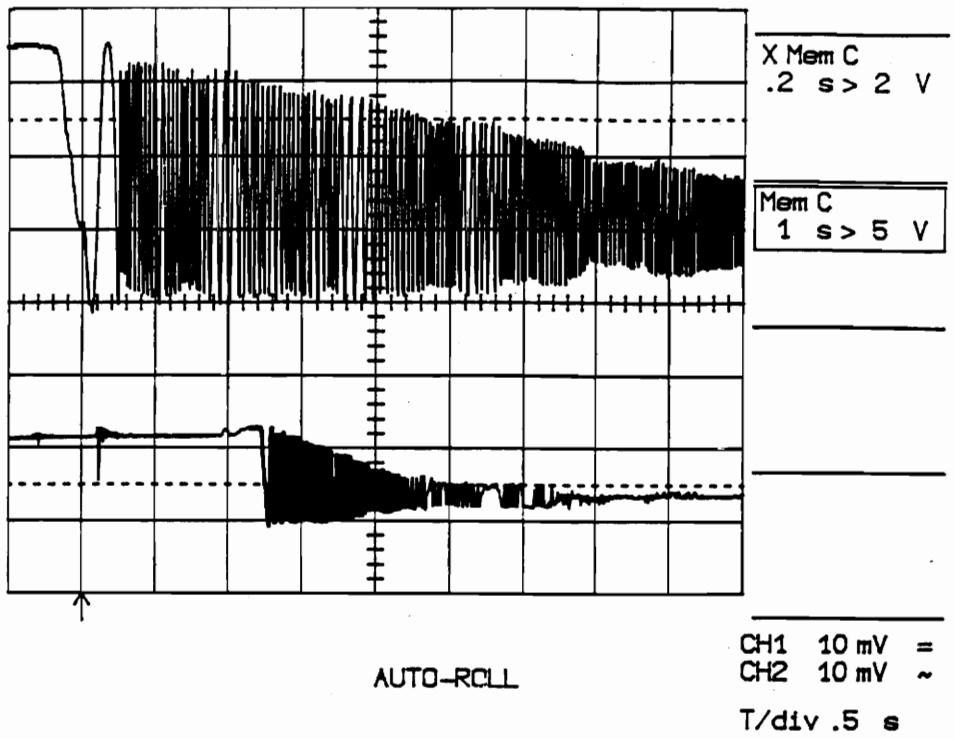

Figure 2.2 Variation of the output intensity of the EFPI for increasing air-gap separation

2.3 Advantages of the EFPI

The EFPI has a number of advantages over other types of interferometric sensors. A major advantage of the EFPI is its small interaction length. This gives it the ability of being a point sensor for effectively monitoring strain, temperature, and vibration. It can be easily bonded onto different materials for sensing applications. Typical specifications for the EFPI are a gage length of 2 mm-3 mm and an air gap separation of about 30μm-40μm. It can be constructed with relative ease and its small size and weight make it very easy to work with. This geometry of the EFPI allows it to be easily embedded in composite materials and therefore it is an ideal candidate for smart structures and smart skins applications. It can be used over a wide frequency range. Limitations on the frequency range are due to the signal processing electronics at the detector end. In addition, it has a sensitivity comparable to other interferometric sensors.

2.4 Limitations of the EFPI

If the input light intensity is sinusoidally modulated at a frequency ω, the photocurrent, i, at the photodetector is given by [2],

$$i = \varepsilon I_0 \alpha \left\{ \begin{array}{l} \mathrm{Cos}\,\phi_d \left[J_0(\phi_s) + 2\sum_{n=1}^{\infty} J_{2n}(\phi_s)\,\mathrm{Cos}(2n\omega t) \right] \\ + \mathrm{Sin}(\phi_d) \left[2\sum_{n=0}^{\infty} J_{2n+1}(\phi_s)\,\mathrm{Sin}\left((2n+1)\omega t\right) \right] \end{array} \right\} \qquad (2.5)$$

where ε is the responsivity of the photodetectors, α is the loss associated with either of the sensing or reference paths, $J_n(\phi_s)$ is the Bessel function of order n and argument, ϕ_s. Here, the differential phase shift in the interferometer may be separated into a signal term

$d\phi$ of amplitude ϕ_s and frequency ω, and a slowly varying phase shift ϕ_d. The differential change in the photocurrent is given by [6],

$$di = \varepsilon I_0 \alpha \sin(\phi_d) \phi_s \sin(\omega t) \tag{2.6}$$

Thus as ϕ_d changes, the output of the interferometer will change. When $\phi_d = m\pi$, $\sin(\phi_d) = 0$. Therefore, the signal vanishes and there is no output from the interferometer. On the other hand, when $\phi_d = (2m+1)\pi/2$, $\sin(\phi_d) = \pm 1$, the signal is maximized. This is known as signal fading in fiber optic interferometers and is shown in Figure 2.3 [2].

The phase condition of $\phi_d = (2m+1)\pi/2$ is known as the quadrature point of the interferometer and it is important to operate the interferometer at this point, to obtain maximum sensitivity.

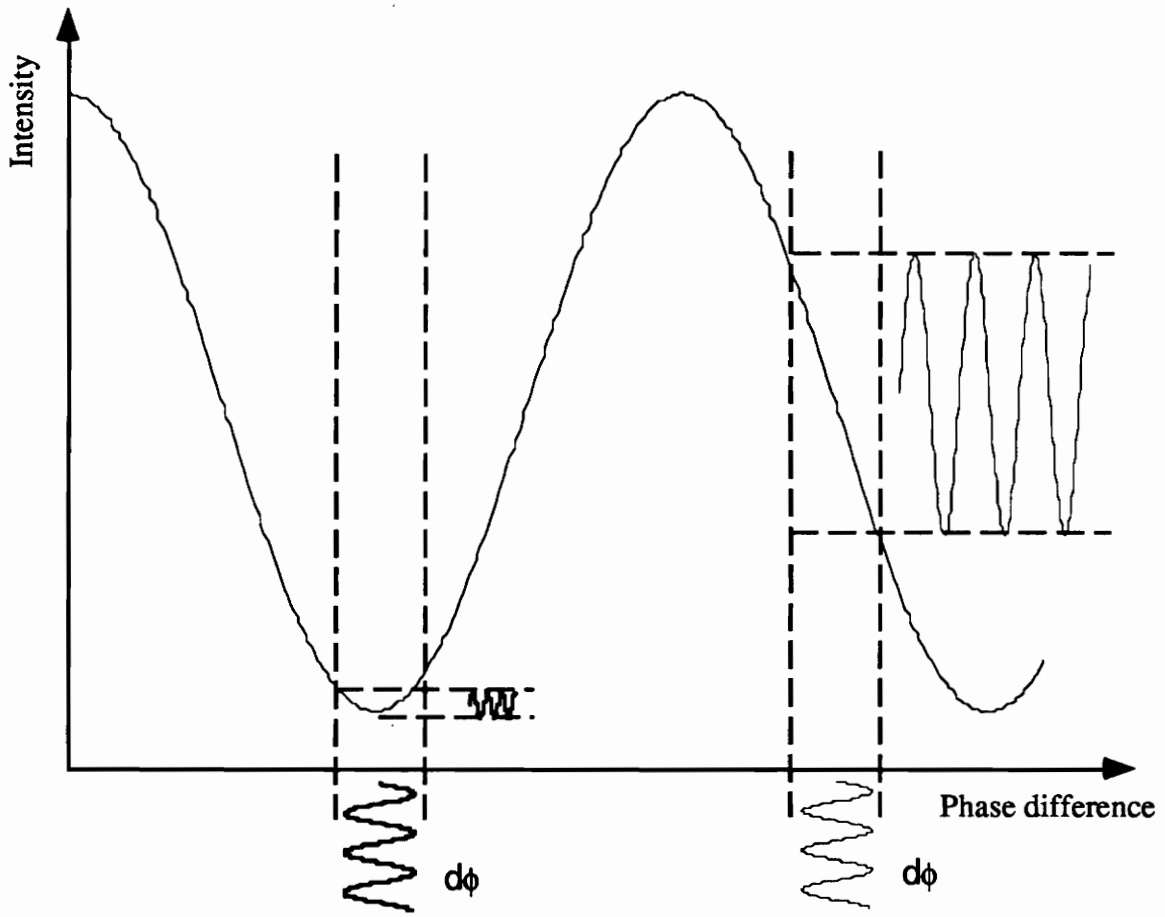

Figure 2.3 Signal fading in fiber interferometers [2]

Thus, the EFPI has to be biased at the quadrature point to achieve maximum sensitivity. This is an obvious limitation and can be overcome by using a quadrature phase shifted scheme [6] which utilizes two sources, two directional couplers, two sensor heads and two detectors. However, a demodulation scheme for sensing dynamic signals from these two outputs would involve complicated electronic circuitry [8].

Another important factor is the source intensity variations. The output of the EFPI, biased at the quadrature point, would still be subject to source intensity variations. In addition, the EFPI output intensity varies with the gap change [8].

Finally, the lead insensitivity of the EFPI does not allow the generation of secondary phase modulation, so spectrum analysis methods cannot be readily applied to the EFPI [8].

Chapter 3. Detection Schemes for Fiber Interferometers

3.1 Basic operation of fiber interferometers

The two light beams from the beam splitter in a two-beam fiber interferometer constitute the reference and the signal beams. These beams can be represented as [9],

$$\begin{aligned} &\text{Reference:} && A_r \exp\left[j(\omega_l t + 2\beta x_r)\right] \\ &\text{Signal} \quad : && A_s \exp\left[j(\omega_l t + 2\beta x_s)\right] \end{aligned} \tag{3.1}$$

where A_r and A_s are the amplitudes of the reference and signal beams, x_r and x_s are the distances traversed by the light beams, β is the propagation constant and is given by $k=2\pi n/\lambda$. λ is the wavelength of operation and n is the index of refraction of the air path. ω_l is the angular frequency of the light source. At the photodetector, the current I_d is given by [9],

$$I_d = \varepsilon\left[1 + K\cos\phi(t)\right] \tag{3.2}$$

where K is the fringe visibility, ε is related to the input optical power and $\phi(t)$ is the time

dependent phase difference between the arms of the interferometer.

The output of fiber interferometers varies with a periodicity of 2π radians. In order for this to operate as a sensor, we require that the output be a unique function of the air gap separation (in the case of Fabry-Perot interferometers).

The displacement sensitivity of the interferometer, $\frac{dI_d}{d\phi}$, varies as sin ϕ (periodically). It is maximum when $\phi = \pm m\pi \pm \frac{\pi}{2}$ and zero when $\phi = \pm m\pi$. As stated in Chapter 2, the maximum sensitivity point is the quadrature point of the sensor. In sensor applications, it is imperative that the fiber interferometer be operated at constant linear sensitivity. Different signal processing techniques are used to achieve this requirement [9].

3.2 Signal processing techniques

The output of the fiber interferometer exhibits variable sensitivity to induced optical phase changes. This is due to the periodicity of the transfer function. As a result of this variable sensitivity, signal fading is produced in interferometers. Therefore, interferometric sensors are usually operated so that the output is a linear function of the optical phase difference. A number of approaches are used to linearize the transfer function of interferometric sensors. These may be classified as:
i) active homodyne ii) passive homodyne iii) heterodyne.

Consider the case of periodic phase modulation. In this case, the optical path length of one of the interferometer arms, is modulated by a signal $d\phi$ of frequency ω_s. The optical phase

difference, $\phi(t)$, between the two beams, may be written as,

$$\phi(t) = \phi_d + d\phi \tag{3.3}$$

where $d\phi = \phi_s \sin \omega_s t$.

Here, ϕ_d is the static phase difference and ϕ_s is the amplitude of the phase change introduced in the interferometer by the modulating signal.

Thus, using equation 3.2, the output current of the photodetector is [9],

$$I_d = \varepsilon \left[1 + K \cos \left(\phi_d + \phi_s \sin \omega_s t \right)\right] \tag{3.4}$$

where

$$\cos \left(\phi_d + \phi_s \sin \omega_s t\right) = \cos(\phi_d) \left[J_0(\phi_s) + 2 \sum_{n=1}^{\infty} J_{2n}(\phi_s) \cos(2n\omega_s t)\right] - \sin(\phi_d) \left[2 \sum_{n=0}^{\infty} J_{2n+1}(\phi_s) \sin\left[(2n+1)\omega_s t\right]\right] \tag{3.5}$$

and J_n is the Bessel function of order n.

3.2.1 Active homodyne

This technique of recovering the input signal ($\phi_s \sin\omega_s t$) which modulates the relative phase in the interferometer, utilizes a piezoelectric based fiber optic modulator. The phase shifter is constructed by winding the optical fiber around a cylindrical piezoelectric transducer. This method allows a phase shift, ϕ_c which is voltage controllable, to be introduced in the

interferometer. The application of a dc voltage in the reference arm results in the interferometer being brought into quadrature [2].

Thus,

$$\begin{aligned} \Delta\phi &= \phi_d - \phi_c + d\phi \\ &= (2m + 1)\frac{\pi}{2} \end{aligned} \tag{3.6}$$

Assuming the value of the fringe visibility, K, as 1, we can write equation 3.4 as,

$$I_d = \varepsilon\left[1 + \cos\left(\phi_d + \phi_s \sin \omega_s t\right)\right] \tag{3.7}$$

Differential combination of this output with the complementary output of the interferometer, results in [2],

$$i = R\,\varepsilon \cos\left(\phi_d + \phi_s \sin \omega t\right)$$

where R is the responsivity of the photodetector.

A first approach, referred to as the low-gain mode of operation [2], is represented as,

$$di = - R\,\varepsilon\, d\phi \tag{3.8}$$

However, as $d\phi$ becomes larger, the output is distorted as the assumption that the interferometer phase $\Delta\phi$ is equal to $(2m + 1)\frac{\pi}{2}$, does not hold. Also, it is seen that the output signal is directly proportional to ε. Thus, any changes in ε affects the output signal.

A second approach [2], ensures the value of $\Delta\phi$ to be $\pi/2$.

$$\begin{aligned}\Delta\phi &= \phi_d + d\phi - \phi_c \\ &= \frac{\pi}{2}\end{aligned} \tag{3.9}$$

Therefore, the output of the interferometer is of the form,

$$i = R\varepsilon \cos(\phi_d + d\phi - \phi_c) \tag{3.10}$$

At quadrature, **i** is zero and deviations from the quadrature condition are given by,

$$\Delta(i)_{\frac{\pi}{2}} = -\varepsilon R (\phi_d + d\phi - \phi_c) \tag{3.11}$$

Now, **i** is zero at the quadrature condition. Also, there is a change of sign as it passes through quadrature. Thus, it can be used as an error signal. This error signal can be driven to zero, by producing an appropriate feedback voltage from **i**. This feedback voltage is applied to the piezoelectric element which controls ϕ_c. Thus, ϕ_c cancels ($\phi_d + d\phi$), driving the error signal to zero. This feedback signal is the integral of **i**, amplified by a gain factor, **g** [2]. Thus,

$$dV_{fb} = g \int_0^{\tau} i(t')\,dt' \tag{3.12}$$

The differential equation for the feedback loop is [2],

$$\frac{dV_{fb}}{dt} + ghR\varepsilon V_{fb} = gR\varepsilon\left(\phi_d + d\phi - \frac{\pi}{2}\right) \tag{3.13}$$

Here, h is the volts-to-radian constant of the piezoelectric element and ghεR is the gain-bandwidth product of the feedback loop. The quadrature condition is,

$$\begin{aligned} \phi_c &= h\, V_{fb} \\ &= \left(\phi_d + d\phi - \frac{\pi}{2} \right) \end{aligned} \tag{3.14}$$

Thus,

$$V_{fb} = \frac{1}{h}\left(\phi_d + d\phi - \frac{\pi}{2} \right) \tag{3.15}$$

The signal information $d\phi$ is present at the feedback voltage. Also, it is linear and therefore, $d\phi$ can be separated from ϕ_d by appropriate filtering.

The two approaches for active homodyne detection for optical phase shifts, are illustrated in Figure 3.1 [2].

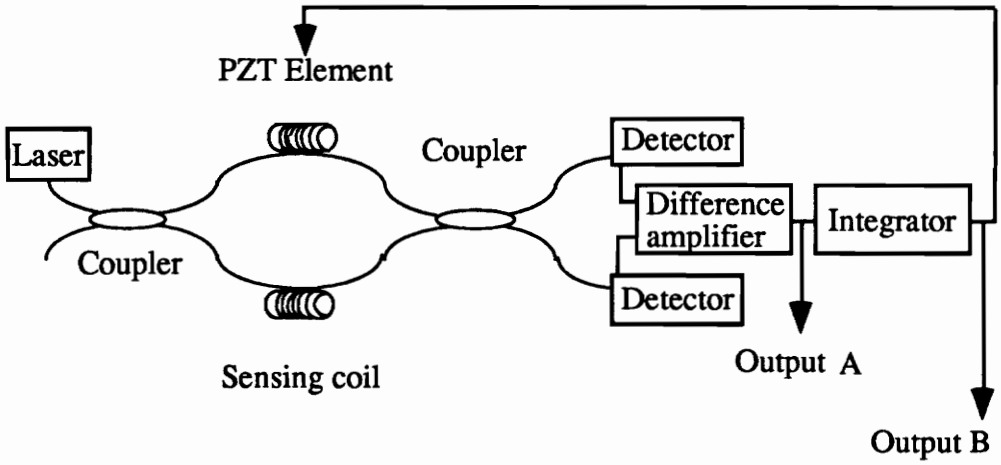

Figure 3.1 Active homodyne demodulation technique. Output A: low-gain approach, Output B: high-gain approach [2]

3.2.1.1 Advantages and limitations of the active homodyne technique

The equations for the active homodyne approach using the high-gain approach show that the output signal is not proportional to ε [2]. Thus any changes in ε, cause a change only in the gain-bandwidth product of the feedback loop. This technique has the advantage of a relative insensitivity to fluctuations in the laser output, variations in the fringe contrast of the interferometer and system attenuation. Another feature of the high-gain approach is that no small-angle approximations have been used in demodulation. Therefore, the output is linear beyond the limit of the low-gain approach. This results in the high-gain approach having a much greater dynamic range. This dynamic range is dependent on the properties of the feedback element and the electronic circuitry.

The active homodyne technique suffers from two drawbacks [2]. First, the piezoelectric element which is used for the feedback element, has a limited dynamic range. This requires the feedback circuit to reset. Typically, this involves a voltage switch of +10V. This results in a downgrading of the interferometers ability to measure signals in the required μV range, which corresponds to μrad phase shifts. In a practical environment, such resets could occur a number of times each second. The resetting operation results in a 'glitch' in the output which severely compromises the ability of the sensor for phase detection. A second disadvantage of this approach, is in multiplexing. A multiplexed system using a single laser is difficult to implement with such a detection scheme, as the laser can keep only one interferometer at quadrature. This would lead to a compromise in the performance of the other sensors.

3.2.2 Passive homodyne technique

Passive homodyne techniques for signal detection do not involve any feedback to the sensor. The basic approach in the passive homodyne technique is to generate two signals that are shifted in optical phase 90^0. This is illustrated in Figure 3.2 [2].

The two outputs can be written as,

$$i = \frac{\varepsilon R}{2}\left(1 + \cos\Delta\phi\right) \tag{3.16}$$

$$i'' = \frac{\varepsilon R}{2}\left(1 + \sin\Delta\phi\right)$$

For a small phase shift $d\phi$,

$$di = \frac{\varepsilon R}{2}\left(d\phi \sin\Delta\phi\right) \tag{3.17}$$

$$di'' = \frac{\varepsilon R}{2}\left(d\phi \cos\Delta\phi\right)$$

The two equations, 3.16 and 3.17, indicate that when one output fades completely, the other output is at a maximum value. Also, either of di or di" are present at the output at any given time. These outputs can be used to prevent signal fading at the output of the interferometer.

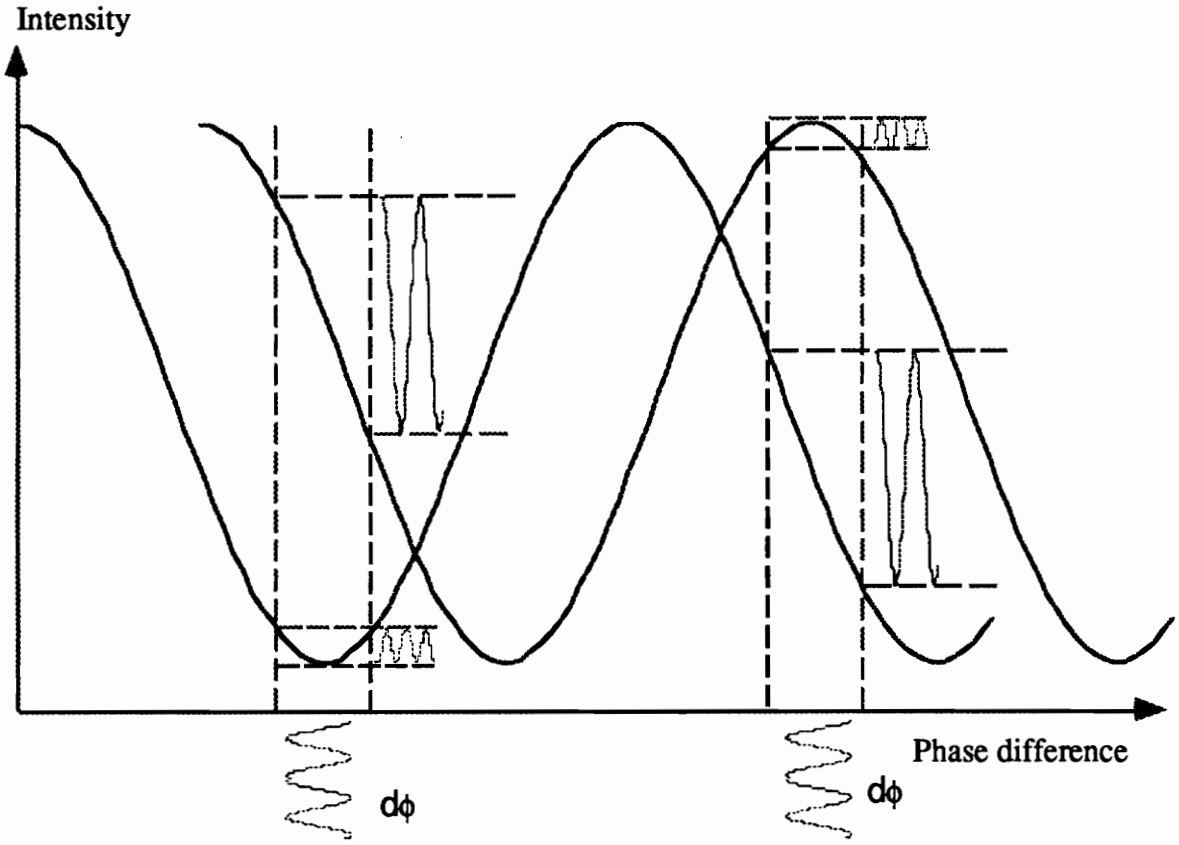

Figure 3.2 Passive demodulation technique utilizing two signals 90 ° out of phase [2]

One method of ensuring that signal fading is not present at the output is to square di and di", add the squares, and then take their square root [2]. Thus,

$$\begin{aligned} \Delta i &= \sqrt{di^2 + di''^2} \\ &= \frac{\varepsilon R}{2} d\phi \end{aligned} \tag{3.18}$$

An alternative method would be to use differentiation and cross multiplication of the two signals [2]. Thus,

$$i\frac{di''}{dt} - i''\frac{di}{dt} = \frac{\varepsilon R}{2}\frac{d(\Delta\phi)}{dt} \tag{3.19}$$

Integration of this equation results in an output that has a linear phase term (signal).

3.2.3 Heterodyne detection

The heterodyne method of signal detection has a number of features which make it attractive for use in fiber optic detection systems [9].

i) The phase detection sensitivity is constant and is independent of the value of ϕ_d. This means that the recovered signal is not subject to signal fading.
ii) The effective phase tracking range is infinite.
iii) The modulating signal can have a very large dynamic range.
iv) This method allows the determination of the direction of fringe motion.

The heterodyne method of signal detection requires that the light in one of the

interferometer arms be frequency shifted with respect to the light in the other arm.

The frequency shifting needed for heterodyne detection requires the use of an acousto-optic modulator. A Bragg cell can be used for such a purpose.

The output signal from the interferometer is given by,

$$I_d = \varepsilon K \cos\left(\omega_b t + \phi_d + \phi_s \sin(\omega_s t)\right) \tag{3.20}$$

where ω_b is the offset frequency. This signal represents a carrier at a frequency ω_b which is phase modulated by ($\phi_d + \phi_s$).

The methods for generating a phase modulated carrier are

i) synthetic heterodyne

ii) pseudo-heterodyne

iii) quadrature recombination heterodyne.

As stated above, the heterodyne detection scheme uses a Bragg cell which is expensive. This results in an increase in the cost of a system utilizing heterodyne detection. The homodyne approach requires feedback to the interferometer for signal detection purposes and this feedback mechanism has inherent disadvantages which have been discussed. In contrast, the next approach to be discussed uses spectrum analysis of the photodetector output. This allows phase measurements in a no-feedback, no-phase bias fiber interferometer.

3.3 Spectrum analysis methods of optical phase detection

Consider the case of an optical fiber interferometer utilizing the active homodyne detectic system. The perturbations introduced in the sensing arm of the interferometer are of a periodic nature, with amplitude A_s and frequency ω_s (eg. a simple harmonic motion, vibrations from a motor, etc.).

The photocurrent, I(t), may be written as [10],

$$I(t) = I_s + I_r + 2\beta\sqrt{I_s I_r}\left\{J_0(2k_0A_s) - 2J_2(2k_0A_s)\cos(4\pi f_s t) + \ldots\ldots\right\} \quad (3.25)$$
$$\cos\theta + 2\beta\sqrt{I_s I_r}\left\{\begin{matrix}2J_1(2k_0A_s)\cos(2\pi f_s t) - 2J_3(2k_0A_s)\\ \cos(6\pi f_s t) + \ldots\ldots\end{matrix}\right\}\sin\theta$$

where I_s is the component of the photocurrent in the sensing arm, I_r is the component of the photocurrent in the reference arm, and β is the homodyne efficiency of the interferometer. Filtering by means of electronic circuitry results in the output consisting only of the harmonic component of order n. The resulting output voltage from this component can be written as [10],

$$V_n = 2\alpha\beta\sqrt{I_s I_r}\begin{pmatrix}\sin\theta\\ \cos\theta\end{pmatrix}J_n(2k_0A_s)\cos(2\pi f_s t) \quad (3.26)$$

where α is a constant of proportionality. The $\begin{pmatrix}\sin\theta\\ \cos\theta\end{pmatrix}$ term takes on the value of $\sin\theta$ or $\cos\theta$ depending on the value of n being odd or even. Equation 3.26 allows us to measure A_s using a number of different spectrum analysis techniques [10], [11].

i) J_{1max} method:

This method requires the value of $\sin\theta=1$. The filtered first-order component has its output voltage given by,

$$V_1 = 2\alpha\beta\sqrt{I_s I_r}\, J_1(2k_0 A_s)\cos(2\pi f_s t) \tag{3.27}$$

From equation 3.27, it is seen that when the Bessel function J_1 attains the first maximum of 0.5819, V_1 has the value V_{1max}. If the system is kept stable for a period of time, we can measure the ratio of V_1 and V_{1max}. This ratio is ,

$$\frac{V_1}{V_{1max}} = \frac{J_1(2k_0 A_s)}{0.5819} \tag{3.28}$$

Thus, a table of Bessel functions can be used to determine A_s.

ii) $J_n(2k_0A_S) = 0$ method:

This method also requires the value of $\sin\theta = 1$. Here, as the value of A_s is steadily increased, a certain value of A_s is reached where $J_n(2k_0A_S)=0$. If this value of A_s is denoted by A_0, then in the vicinity of A_0, the driving voltage to the piezoelectric element is proportional to the vibration amplitude A_s. This allows the determination of a small amount of deviation from A_0.

iii) (J_1/J_2) or (J_1/J_3) method:

The (J_1/J_2) scheme of detection utilizes successive setting of $\sin\theta=1$ and $\cos\theta=1$, thus allowing the measurement of two voltages V_1 and V_2 at frequencies f and 2f respectively. The ratio of V_1 and V_2 can be written as,

$$\frac{V_1}{V_2} = \frac{J_1(2k_0A_s)}{J_2(2k_0A_s)} \tag{3.29}$$

The above ratio is valid so long as the coefficients of the Bessel function in equation 3.26 do not change.

In a similar way, the method employing (J_1/J_3) will yield the ratio,

$$\frac{V_1}{V_3} = \frac{J_1(2k_0A_s)}{J_3(2k_0A_s)} \tag{3.30}$$

iv) J_n recurrence formula method:

This method of spectrum analysis uses the recurrence formula for Bessel functions. This formula is given by,

$$2nJ_n(u) = u\{J_{n-1}(u) + J_{n+1}(u)\} \quad (n = 1,2,3,..) \tag{3.31}$$

The required value of $\sin\theta$ is equal to 1.

Utilizing $u=2k_0A_s$, the relation for A_s can be written as,

$$A_s = \left(\frac{1}{2k_0}\right)\sqrt{\frac{(4n\,(n+1)(n+2)V_{n+1})}{((n+2)V_{n-1} + 2(n+1)V_{n+1} + nV_{n+3})}} \tag{3.32}$$

In the above equation, the required value for sinq=1. This results in the ability to measure all the individual components at the same time, which finally results in the determination of A_s.

v) $J_1..J_4$ method:

The measurement of dynamic phase changes can be accomplished by using the $J_1..J_4$ technique of spectrum analysis [11]. This method can be used to make phase measurements in a no-feedback, no phase-bias optical fiber interferometer. It also utilizes the J_n recurrence relation to determine the value of the phase shift, x, as,

$$x^2 = \frac{4i(i+1)V_iV_{i+1}}{(V_i + V_{i+2})(V_{i-1} + V_{i+1})} \tag{3.33}$$

In equation 3.33, the value of i is greater than 1. The voltage component V_i, is given by,

$$V_i = 2BGJ_i(x) \tag{3.34}$$

where i is the i^{th} frequency component. G is cos ϕ_0 (sin ϕ_0) for i even (odd) and $\phi_0(t)$ denotes the random phase drifts. For i=2, we can write equation 3.33 as,

$$x^2 = \frac{24V_2V_3}{(V_2 + V_4)(V_1 + V_3)} \tag{3.35}$$

The phase measurements obtained using this technique, are not affected by fluctuations in light source intensity, random phase drifts, and variations in the fringe contrast [11]. Thus, there is no need for biasing the sensor at the quadrature condition. Also, stabilization of the source intensity and polarization control to maximize the fringe contrast, are not required. This is in sharp contrast to the $\mathbf{J_{1max}}$ technique wherein additional electronic and optical components are required to obtain the above benefits. There are inherent inaccuracies in the $(\mathbf{J_1/J_2})$ method as it has a stringent requirement that the coefficients of the Bessel functions do not change between the two phase settings. The $(\mathbf{J_1/J_3})$ method also needs a phase setting and an inversion of the Bessel function to obtain the modulation depth. On the other hand, the $\mathbf{J_1..J_4}$ method can be implemented by bandpass filtering of V(t) at four successive harmonics and evaluating equation 3.35.

The $\mathbf{J_{1max}}$ technique is known to be the most sensitive technique for the measurement of phase shifts. However, this method requires that the first maximum of J_1 be reached before any measurements can be taken. The $\mathbf{J_1..J_4}$ method is self-consistent and is superior to the $\mathbf{J_{1max}}$ method over the range x=0.1-1.83 rad and for higher values of x [11].

Chapter 4. The Split-cavity Cross-coupled Extrinsic Fiber Interferometer

4.1 Introduction

The Fabry-Perot configuration of fiber optic interferometric sensors [12],[13] has a sensitivity double that of the Mach-Zehnder configuration and uses a single fiber instead of two fibers, as compared to the latter. The Fabry-Perot fiber interferometer has been demonstrated with both single mode [14] as well as multimode fiber. A higher sensitivity to physical measurands in sensor applications and a large free spectral range in wavelength selective demultiplexers has been demonstrated by coating the fiber end faces with dielectric reflective layers [15] or by butt-coupling the fiber endface with a high quality mirror. In the intrinsic version, the two end faces of a single fiber are used as the reflectors whereas in the extrinsic version, the Fabry-Perot cavity is formed between the ends of the single mode fiber and a multimode fiber, inserted into a hollow core fiber from its opposite ends. The construction and operation of the Extrinsic Fabry-Perot Interferometer (EFPI) is described in Chapter 2 of this thesis. This extrinsic version acts as an effective point sensor for application in strain, vibration, and temperature measurements. Several demonstrations of

the EFPI have been reported [16] wherein the sensor head is embedded in composite panels or such other rigid substrates.

For the maximization of the sensitivity, a stringent requirement of biasing the EFPI at the quadrature point is imposed during fabrication and subsequent use. In order to overcome this limitation, a quadrature phase shifted method was devised wherein two signals out of phase by 90^0 were obtained by using two sources, two directional couplers, two sensor heads and two detectors. The typical demodulation scheme [17] for sensing dynamic signals from these two outputs would involve complicated electronic circuitry.

In contrast, there exists a generic class of spectrum analysis methods [11], [18], [19] that provide a linear, direct and self consistent readout of the dynamic phase shift in homodyne interferometers. These methods are unaffected by random phase drifts, visibility variations or source intensity fluctuations, thus these eliminate the need for interferometer feedback or source stabilization. A brief description of such methods is described in Chapter 3 of this thesis. The $J_1..J_4$ method has a detectability of 0.1 rad, whereas the $J_0.J_2$ method, which utilizes a secondary phase modulation, can measure a minimum of 0.01 rad.

In addition, there exists a passive homodyne technique [20] that uses a phase generated carrier leading to a μradian phase sensitivity. The generation of a secondary phase modulation is readily possible in sensor configurations with extended interaction length. However, in the case of the EFPI, the lead insensitivity to random phase drifts does not allow such a modulation except

(a) at the sensor head itself, or

(b) source frequency modulation which is converted into phase modulation by the path difference at the sensor head itself.

In applications where the sensor head is embedded in some material, secondary phase modulation at the sensor head is ruled out because the presence of electrical power at the sensing point is undesirable. Also, the cable carrying power to that point would pick up stray signals. Frequency modulation of the source is limited by the cross-sensitivity between the output power and the frequency in response to a change in the injection current. More importantly, the output of the EFPI biased at the quadrature point would still be subject to source intensity variations, notwithstanding the fact that the EFPI output intensity varies with the air gap change.

The optical fiber sensor developed and demonstrated in this thesis is called the Split-cavity Cross-coupled Extrinsic Fiber Interferometer (SCEFI) [8],[21]. This sensor is essentially a new configuration of the EFPI. It utilizes two EFPI sensor heads in a split-cavity cross-coupled arrangement on a single directional coupler. The secondary phase modulation acts on the modulator head on the same side of the coupler as the source, while the signal is detected by the sensor head remotely placed from the source.

This arrangement has several advantages such as:

(a) elimination of the need of phase bias,

(b) elimination of the effect of intensity variation with air-gap,

(c) small signal detectability by secondary phase modulation,

(d) detection of static as well as dynamic signals,

(e) simple multiplexing of two EFPI's on a single coupler.

4.2 Optical configuration of SCEFI

The SCEFI is shown in Figure 4.1. The light from the laser diode on port A is split at the coupler and guided through port B. At port B, the first reflection from the single mode fiber end and the subsequent reflection from the multimode fiber end interfere to form a zero order fringe pattern. This recombined light from the sensor EFPI head is re-injected into the port D where again another EFPI is formed by the single mode - multimode fiber junction at the hollow core fiber. The secondary phase modulation is induced at this head by means of a piezoelectric or magnetostrictive transducer. The light emerging from the port C would thus consist of four beams between each pair of which interference would occur. This is in contrast to the earlier version of the EFPI wherein only the sensor EFPI head on port B was utilized, with the single mode fiber end on port C terminated in index matching gel to reduce unwanted reflection. The output from port D would then have been only two interfering beams. If these beams are out of quadrature, the signal at the output would fade resulting in a sensitivity that is dependent on the value of the phase difference.

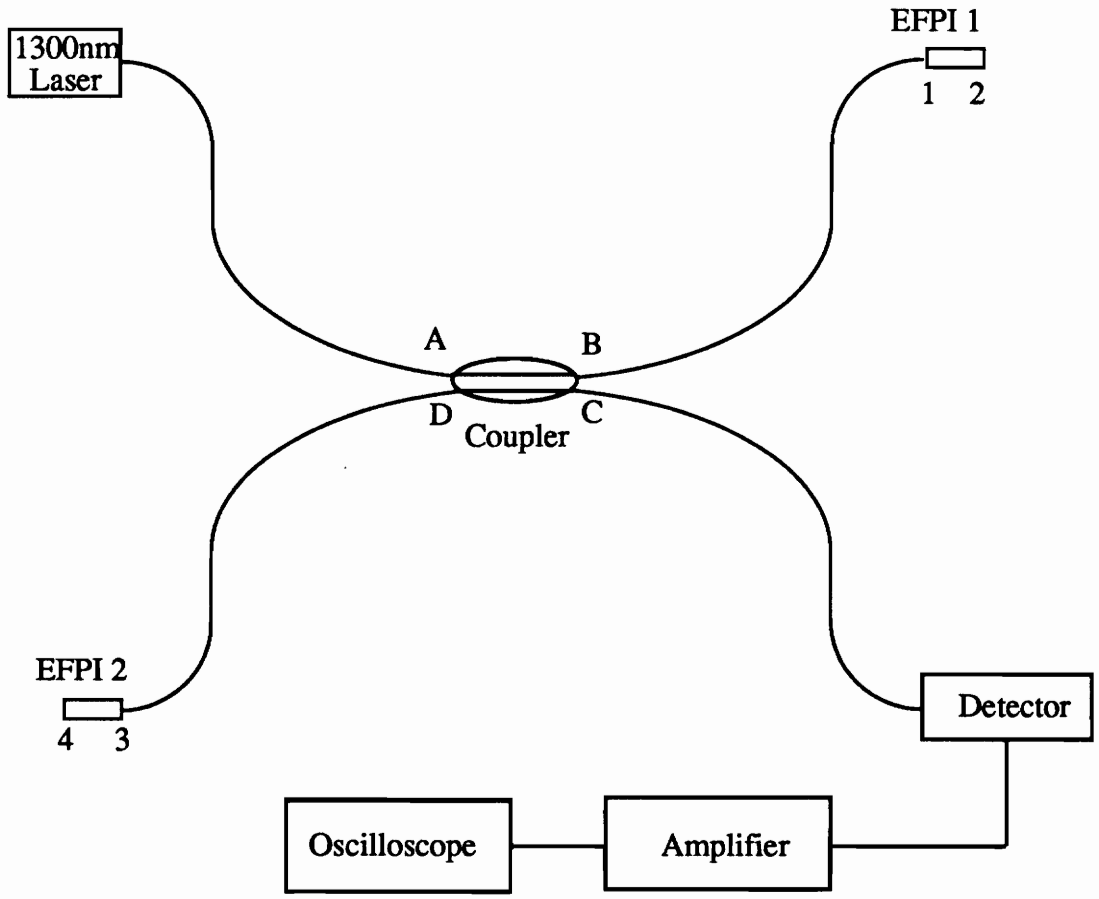

Figure 4.1 Schematic of the Split-cavity Cross-coupled Extrinsic Fiber Interferometer

4.3 Theory and signal detection

The intensities of the four beams at the output of the SCEFI as read from port C, can be represented as I_{13}, I_{14}, I_{23}, and I_{24}. Here I_{ij} represents the intensity of the light reflected first from the endface i and subsequently from the endface j. The higher order reflection terms such as I_{ijk} and I_{ijkl} are considered negligible as the Fresnel reflection coefficient is only 4% and the directional coupler cuts down the intensity by 3 dB on every pass. Thus, there would be six interference terms that form into three distinct pairs. For dynamic phase shifts, the time-dependent output voltage at D1, due to the four-beam interference is [22],[23],

$$V(t) = M + N\begin{pmatrix}\cos\left[2(\phi_s + \phi_c + \phi_a + \phi_b)\right] + \\ \cos\left[2(\phi_s + \phi_a - \phi_c - \phi_b)\right] + \\ 2\cos\left[2(\phi_s + \phi_a)\right] + 2\cos\left[2(\phi_c + \phi_b)\right]\end{pmatrix} \tag{4.1}$$

where $M=2V_o$ and $N=2V_ob$. V_o is the photovoltage due to the average Fresnel-reflected intensity of the fiber output and b is the fringe visibility. Also, $\phi_s=x\sin\omega_s t$, $\phi_c=y\sin\omega_c t$, where x and y are the phase modulation depths, ω_s and ω_c are the angular frequencies of the signal and the carrier, ϕ_a is the random phase drift at the sensor head and ϕ_b is the random phase drift at the modulator head.

Under the assumptions that i) both ϕ_s and ϕ_c are dynamic, and ii) when recording V(t), the time scale of recording V(t) is larger than the largest time scale variation of ϕ_a and ϕ_b, equation 4.1 can be rewritten as,

$$V(t) = M + 2N\begin{pmatrix}\cos[2(\phi_s + \phi_c + \phi_a + \phi_b)] + \\ \cos[2(\phi_s + \phi_a)] + \cos[2(\phi_c + \phi_b)]\end{pmatrix} \quad (4.2)$$

The modulation depths, x and y, are the parameters to be measured and related to the physical quantity inducing them. It is seen from equation 4.1 that the output of the SCEFI would contain intermodulation frequency components whose amplitude would be dependent on the addition of the phase bias at the sensor head, as well as the modulator head. Thus the phase bias applied at the modulator head can be adjusted so that the total phase is set at the quadrature point without affecting or controlling the naturally imposed phase drift at the sensor head. However, it is known that when spectrum analysis methods of linear phase detection are used, there is no need to set the phase bias to any value. As the output for the SCEFI contains three distinct terms as seen in equation 4.1 in contrast to a single term in simple two beam interference, a new spectrum analysis scheme based on the generic Bessel recurrence relation technique, was devised and used for linear phase detection.

4.3.1 New spectrum analysis scheme for the SCEFI

The four interference beams, I_{13}, I_{14}, I_{23}, and I_{24}, can be combined as: i) I_{13}, I_{14} ii) I_{13}, I_{23} iii) I_{13}, I_{24} iv) I_{14}, I_{24} v) I_{14}, I_{23} vi) I_{24}, I_{23}. The random phase drifts are introduced when the fiber stretches due to temperature and pressure fluctuations.

Consider the term, $\cos[2(\phi_s + \phi_c + \phi_a + \phi_b)]$

Let $\phi = \phi_a + \phi_b$

Then $\cos\left[2(\phi_s + \phi_c + \phi_a + \phi_b)\right]$ can be written as,

$$\cos\left\{2x\sin(\omega_s t) + 2y\sin(\omega_c t) + 2\phi\right\} = \cos\left(2x\sin(\omega_s t)\right). \tag{4.3}$$

$$\cos\begin{pmatrix} 2y\sin(\omega_c t) \\ + 2\phi \end{pmatrix}$$

$$- \sin\left(2x\sin(\omega_s t)\right)\sin\begin{pmatrix} 2y\sin(\omega_c t) \\ + 2\phi \end{pmatrix}$$

$$= \cos\left(2x\sin(\omega_s t)\right)\begin{Bmatrix} \cos\left(2y\sin(\omega_c t)\right)\cos 2\phi \\ - \sin\left(2y\sin(\omega_c t)\right)\sin 2\phi \end{Bmatrix} \tag{4.4}$$

$$- \sin\left(2x\sin(\omega_s t)\right)\begin{Bmatrix} \sin\left(2y\sin(\omega_c t)\right)\cos 2\phi \\ + \cos\left(2y\sin(\omega_c t)\right)\sin 2\phi \end{Bmatrix}$$

We now use the following Bessel function identities to expand equation 4.4.

$$\begin{aligned} \cos\left(x\sin\theta\right) &= J_0(x) + 2J_2(x)\cos 2\theta + \ldots\ldots \\ \sin\left(x\sin\theta\right) &= 2J_1(x)\sin\theta + 2J_3(x)\sin 3\theta + \ldots\ldots \end{aligned} \tag{4.5}$$

Using equation 4.5, we can expand equation 4.4 as,

$$= \left[J_0(2x) + 2J_2(2x)\cos 2\omega_s t\right]\begin{Bmatrix} \left[J_0(2y) + 2J_2(2y)\cos 2\omega_c t\right]\cos 2\phi - \\ \left[2J_1(2y)\sin\omega_c t + 2J_3(2y)\sin 3\omega_c t\right]\sin 2\phi \end{Bmatrix} \tag{4.6}$$

$$-\left[2J_1(2x)\sin\omega_s t + 2J_3(2x)\sin 3\omega_s t\right]\begin{Bmatrix} \left[2J_1(2y)\sin\omega_c t + 2J_3(2y)\sin 3\omega_c t\right]\cos 2\phi \\ + \left[J_0(2y) + 2J_2(2y)\cos 2\omega_c t\right]\sin 2\phi \end{Bmatrix}$$

The form of equation 4.6 allows us to formulate expressions for the different intermodulation components. The components of interest are:

i) $V(|f_s \pm f_c|)$

ii) $V(|f_s \pm 2f_c|)$

iii) $V(2|(f_s \pm f_c)|)$

iv) $V(|2f_s \pm f_c|)$

v) $V(f_s)$

vi) $V(3f_s)$

We shall now proceed to formulate expressions for each of the above frequency components. In the equations developed below, $P=\cos 2\phi$ and $Q=\sin 2\phi$, are used to further simplify the notation.

1) Let A denote the amplitude of the frequency component at $f_s \pm f_c$. Thus,

$A = V(|f_s \pm f_c|)$

The terms in equation 4.6 that contribute to the above frequency components are:

$$\left[2J_1(2x)\sin\omega_s t\right] . \left[2J_1(2y)\sin\omega_c t\right]\cos 2\phi$$

$$= 4J_1(2x)J_1(2y)\,\frac{1}{2}\left[\cos(\omega_s - \omega_c)t - \cos(\omega_s + \omega_c)t\right]\cos 2\phi$$

Using equation 4.2, we can write the expression for A as,

$$A = 4NPJ_1(2x)J_1(2y) \qquad (4.7)$$

2) Let B denote the amplitude of the frequency component at $f_s \pm 2f_c$. Thus,
$B = V(|f_s \pm 2f_c|)$

The terms in equation 4.6 that contribute to the above frequency components are:

$$[2J_1(2x)\sin\omega_s t] \cdot [2J_2(2y)\cos 2\omega_c t]\sin 2\phi$$

$$= 4J_1(2x)J_2(2y)\frac{1}{2}[\sin(\omega_s + 2\omega_c)t + \sin(\omega_s - 2\omega_c)t]\sin 2\phi$$

Using equation 4.2, we can write the expression for B as,

$$B = 4NQJ_1(2x)J_2(2y) \qquad (4.8)$$

3) Let C denote the amplitude of the frequency component at $2(f_s \pm f_c)$. Thus,
$C = V(2|f_s \pm f_c|)$

The terms in equation 4.6 that contribute to the above frequency components are:

$$[2J_2(2x)\cos 2\omega_s t] \cdot [2J_2(2y)\cos 2\omega_c t]\cos 2\phi$$

$$= 4J_2(2x)J_2(2y)\frac{1}{2}[\cos 2(\omega_s + \omega_c)t + \cos 2(\omega_s - \omega_c)t]\cos 2\phi$$

Using equation 4.2, we can write the expression for C as,

$$C = 4NPJ_2(2x)J_2(2y) \qquad (4.9)$$

4) Let D denote the amplitude of the frequency component at ($2f_s \pm f_c$). Thus,

$D = V(|2f_s \pm f_c|)$

The terms in equation 4.6 that contribute to the above frequency components are:

$$[2J_2(2x)\cos 2\omega_s t].[2J_1(2y)\sin 2\omega_c t]\sin 2\phi$$

$$= 4J_2(2x)J_1(2y)\frac{1}{2}[\sin(2\omega_s + \omega_c)t - \sin(2\omega_s - \omega_c)t]\sin 2\phi$$

Using equation 4.2, we can write the expression for D as,

$$D = 4NQJ_2(2x)J_1(2y) \qquad (4.10)$$

The derivations for the expressions of A, B, C and D utilized terms in the equation 4.6. In addition, equation 4.2 can be utilized to develop expressions for the amplitudes at f_s and $3f_s$.

The term $[\cos 2(\phi_s + \phi_a) + \cos 2(\phi_c + \phi_b)]$ can be expanded into its individual terms. The first term can be written as,

$$\cos 2(\phi_s + \phi_a) = \cos 2(x \sin \omega_s t + \phi_a)$$

$$= \cos(2x \sin\omega_s t)\cos(2\phi_a) - \sin(2x \sin\omega_s t)\sin(2\phi_a)$$

$$= \cos(2x \sin\omega_s t)\cos(2\phi_a) - [2J_1(2x)\sin\omega_s t + 2J_3(2x)\sin 3\omega_s t]\sin(2\phi_a) \qquad (4.11)$$

5) Let E denote the amplitude of the frequency component at f_s. Thus,

$E = V(f_s)$

The terms in equations 4.6 and 4.11, that contribute to the above frequency component are:

$$\left[2J_1(2x)J_0(2y)\sin 2\phi + 2J_1(2x)\sin(2\phi_a)\right]\sin\omega_s t$$

$$= 2J_1(2x)\left[J_0(2y)Q + \sin(2\phi_a)\right]$$

Using equation 4.2, we can write the expression for E as,

$$E = 4NJ_1(2x)\left[QJ_0(2y) + \sin(2\phi_a)\right] \qquad (4.12)$$

6) Let F denote the amplitude of the frequency component at $3f_s$. Thus,

$F = V(3f_s)$

The terms in equations 4.6 and 4.11, that contribute to the above frequency component are:

$$\left[2J_3(2x)\sin 3\omega_s t\, J_0(2y)\sin(2\phi) + 2J_3(2x)\sin(2\phi_a)\sin\omega_s t\right]$$

$$= 2J_3(2x)\left[QJ_0(2y) + \sin 2\phi_a\right]\sin(3\omega_s t)$$

Using equation 4.2, we can write the expression for E as,

$$F = 4NJ_3(2x)\left[QJ_0(2y) + \sin(2\phi_a)\right] \qquad (4.13)$$

The equations 4.7, 4.8, 4.9, 4.10, 4.12, 4.13. are used to formulate an expression for determining the phase shift 2x. The new spectrum analysis scheme is based on these equations. This new scheme allows the determination of the sensor phase shift from the SCEFI output by making measurements at the different frequencies specified above and using the expression developed below.

Consider the expression,

$$2x = \frac{4\sqrt{(CD)}}{\sqrt{AB}\left[1 + \frac{F}{E}\right]} \tag{4.14}$$

$$= \frac{4\sqrt{4NP\,J_2(2x)\,J_2(2y)\;4\,NQ\,J_2(2x)\,J_1(2y)}}{4N\sqrt{PQ}\,J_1(2x)\sqrt{J_1(2y)}\sqrt{J_2(2y)}\left[1 + \frac{J_3(2x)}{J_1(2x)}\right]}$$

$$= \frac{4\,J_2(2x)}{J_1(2x)\left[1 + \frac{J_3(2x)}{J_1(2x)}\right]}$$

Thus, the value of x is,

$$2x = \frac{4\,J_2(2x)}{J_1(2x) + J_3(2x)}$$

In general,

$$x = \frac{2\,J_n(x)}{J_{n-1}(x) + J_{n+1}(x)} \tag{4.15}$$

Therefore, we call the measurement of the sensor phase shift, 2x, using equation 4.14, as the $J_1.J_3$ method. The common factors in equation 4.14 such as random phase drift, source intensity variation, and visibility changes are eliminated by cancellation. This provides a self-consistent linear readout of the phase shift.

Chapter 5. Experimental Configuration, Results and Discussion

5.1 Experimental arrangement

The SCEFI was fabricated on a fused fiber directional coupler as shown in Figure 5.1 [8]. The single mode fiber ends of the sensor and modulator heads were inserted into the open hollow core fiber ends so that they were freely supported. The distal ends of the hollow core fiber were fused to the multimode fiber ends and the hollow core fiber - multimode fiber junctions were bonded with a low modulus epoxy onto thin piezofilms driven by electrical signals. No fixation was made at the single mode fiber ends which were supported by a metal plate attached to a three-axis translation stage allowing fine adjusting of the air gap length in the sensor and modulator heads.

The piezofilm acted as a suitable test phase modulator to generate appreciable phase shifts with a low drive voltage. The freedom of movement gained by using the freely supported condition was accompanied by random phase drifts due to the non uniform vibration of the piezofilm supported freely on a thin strip of hard board. The fiber ends within the two EFPI heads were not coated with any reflective material and hence the interference was

essentially by Fresnel reflection.

The output of the photodetector was amplified and fed into a digital oscilloscope with the FFT option. This allowed the determination of the voltage amplitudes at the several frequencies indicated in equation 4.14.

For detection purposes, two different detector configurations were used and these are shown in Figure 5.2.

Figure 5.2a uses an additional coupler before the laser input to the SCEFI. Detector D1 is used to monitor the phase shifts at the sensor head alone, while detector D2 is used to monitor the SCEFI output.

A convenient arrangement of a support system for testing the SCEFI was readily available and is shown in Figure 5.2b. This system was utilized for directly monitoring the counter propagating beams at the detectors D3 and D4. Both these detectors monitor the SCEFI output simultaneously.

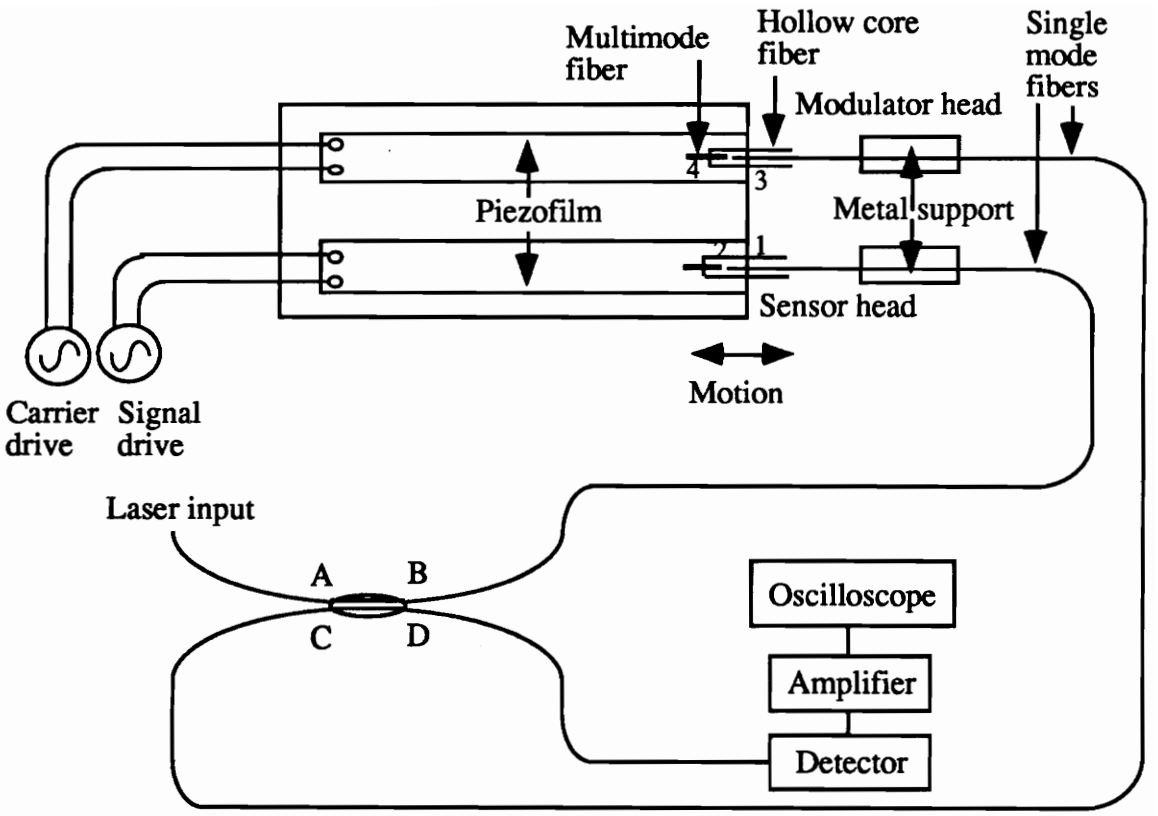

Figure 5.1 Experimental arrangement of the SCEFI

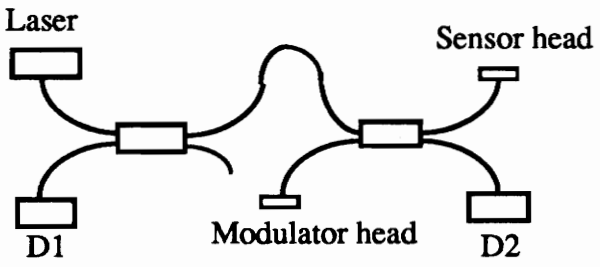

Figure 5.2 a) SCEFI detection using an additional coupler

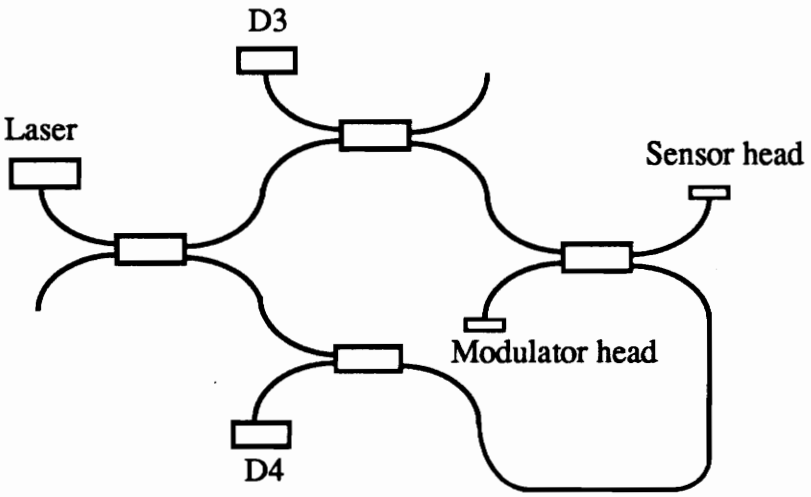

Figure 5.2 b) Two detector support system for the SCEFI

5.2 Results and discussion

In the experiment, the sensor head of the SCEFI was driven at 4.2 kHz and the modulator head at 4.8kHz. The output at the detectors D3 and D4 are shown in Figures 5.3a and 5.3b for two arbitrary sampling instants. The output at both the detectors show a strong frequency peak at the difference frequency of 600 Hz.

Figures 5.4a and 5.4b show the output at the detectors D1 and D2 in the frequency domain, for two arbitrary sampling instants. The modulation at the modulator head was 3.5 kHz and that at the sensor head was 3 kHz.

The output of the SCEFI as shown in Figures 5.3 and 5.4 shows a strong co-relation with the theoretical model developed for the SCEFI in Chapter 4. The strong peaks at the difference frequencies of 600 Hz and 500 Hz and the other intermodulation frequencies indicated in equations 4.14 and 4.16 confirm the validity of the four beam interference model used here for the SCEFI mechanism.

The fact that the SCEFI would be affected by the addition of the drifts in the sensor and modulator heads was verified by comparing it with the output of a single EFPI concurrently. This was implemented by removing the voltage drive to the modulator head, with the sensor head alone being driven at 3 kHz. The output at the detector D1 is affected by the phase drift in the sensor head alone, while the output of the SCEFI at D2 is affected by the additions of the drifts at the sensor and modulator heads. This additional drift, induced at the modulator head, can be utilized to stabilize the SCEFI output at D2 by means of electronic feedback to the modulator head, which will control the total phase bias and maintain itself at 90°. This is shown in Figure 5.5 which illustrates the beneficial effects of

the addition of the drifts at the two EFPI heads; namely that the control of the total phase drift by an integral feedback to the modulator head would lead to remote sensor stabilization. Figure 5.5a and 5.5b show that, with the signal applied to the sensor head alone, the outputs of the single EFPI (at D1) and the SCEFI (at D2) show identical amplitude peaks at the sensor modulation of 3 kHz. But when the modulator head signal is turned on, the SCEFI output at detector D2 is comprised of the addition of both the modulations, while detector D1 is still comprised of the sensor head modulation signal only. This is shown in Figure 5.5c.

Figure 5.6 shows the SCEFI output at D4 for a signal frequency of 2.99 kHz and a modulator frequency of 3.69 kHz, for two arbitrary sampling instants. The phase shifts determined from equation 4.14 were 1.397 rad and 1.556 rad respectively. The phase shift averaged over 10 trials was 1.417±0.107 rad from the SCEFI, while that from the single EFPI was 1.419±0.083 rad (using $J_1..J_4$ method). This excellent agreement between the several phase measurements confirmed the applicability of the new spectrum analysis scheme for the SCEFI.

The phase shifts measured for the plots in Figure 5.4 were 2.196 and 2.341 rad using the new $J_1.J_3$ method developed for the SCEFI [21].

The phase shift measured for the plot in Figure 5.5 b) was 2.134 rad for the SCEFI and 2.047 rad for the single EFPI. For Figure 5.5 c), the phase shift measured was 2.269±0.049 rad using the $J_1..J_4$ method directly to the SCEFI output [21].

The SCEFI was adjusted so that the difference frequency peak was much stronger than the other peaks. This was done to enable the study of the SCEFI output as a function of the

injection current applied to the laser diode. It is known that the emission frequency/ wavelength of the laser diode varies with the injection current. Thus, one could tune the wavelength to bias the interferometer at the quadrature point for a given gap length in the EFPI heads.

Figure 5.7 shows the time domain and frequency domain plots of the SCEFI output at D4 for a signal frequency of 4.2 kHz and a modulation frequency of 4.8 kHz. The depth of modulation at the difference frequency is clear from the time domain plot where there are eight small peaks, corresponding to 4.8 kHz, within the slowly varying 600 Hz modulation. The injection current for these plots was 28.2 mA and the amplitude at the difference frequency of 600 Hz. was 141 mV.

Figure 5.8 shows the frequency spectra (at D4) for two different currents of 29.8 mA and 30.1 mA. The sharp jump in the amplitude for a relatively small change in the injection current confirms the sensitivity of the SCEFI to a change in wavelength. This indicates the possible use of the SCEFI as a split cavity etalon with a variable air gap at the modulator head for spectral filters in WDM systems [15], [24].

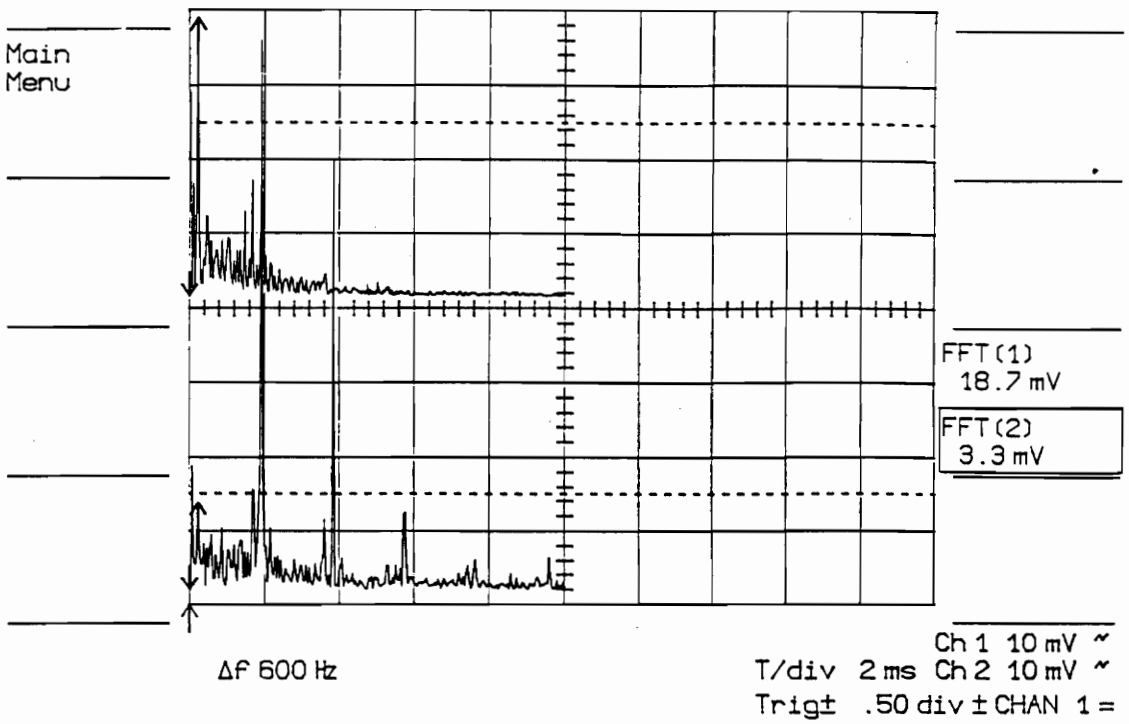

Figure 5.3 a) FFT of the SCEFI output at D4 (lower trace) and D3 (upper trace) at an arbitrary sampling instant.

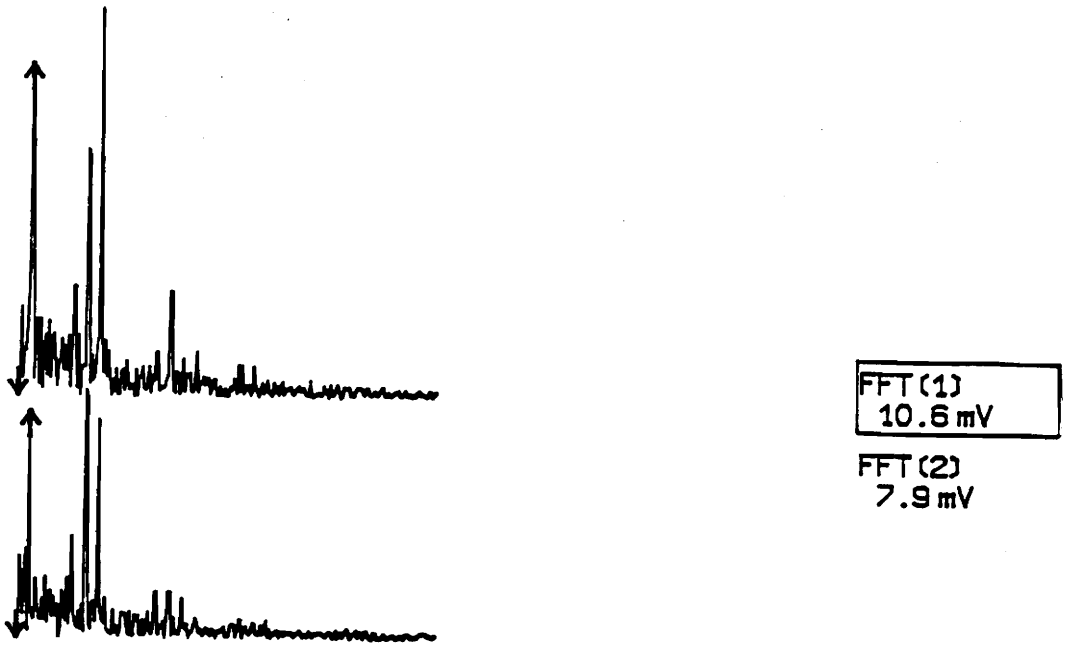

Figure 5.3 b) FFT of the SCEFI output at D4 (lower trace) and D3 (upper trace) at a different sampling instant.

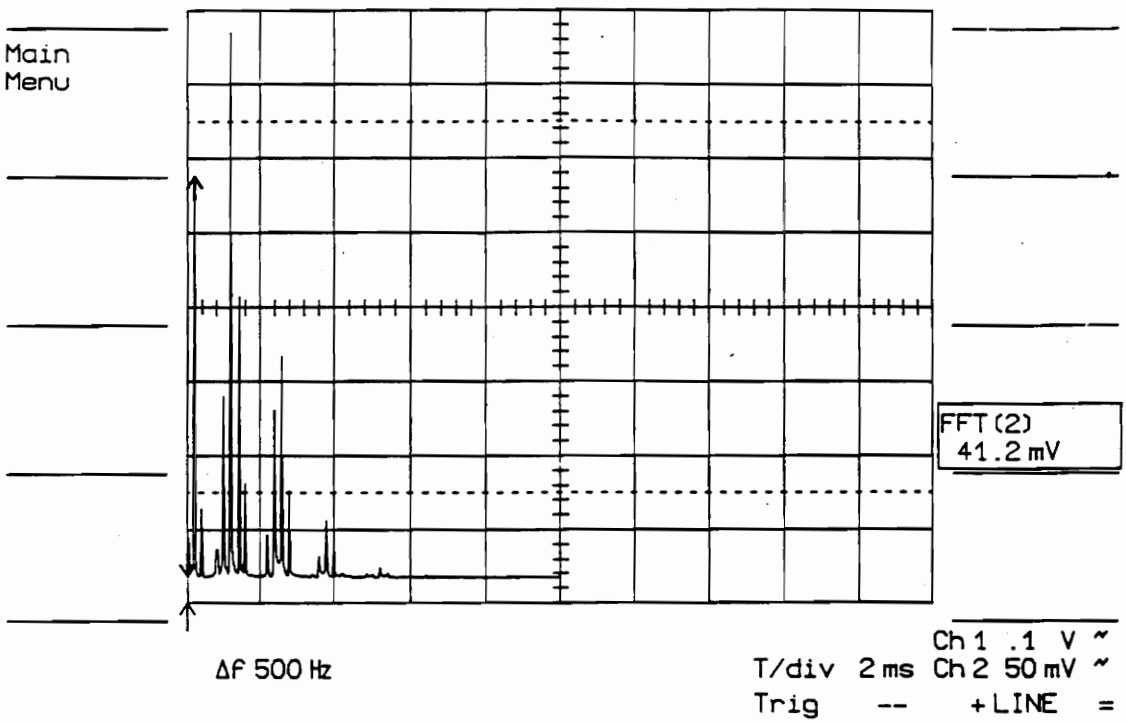

Figure 5.4 a) FFT of the SCEFI output at D2 for a difference frequency of 500 Hz.

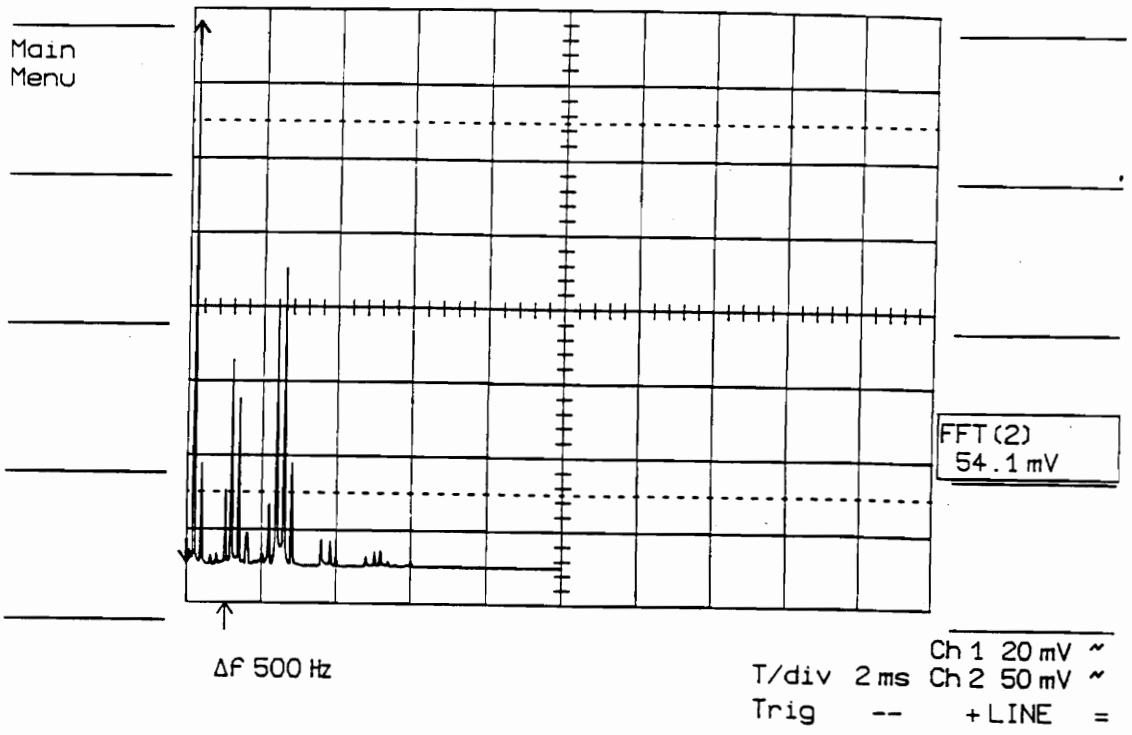

Figure 5.4 b) FFT of the SCEFI output at D2 for a difference frequency of 500 Hz, at a different sampling instant.

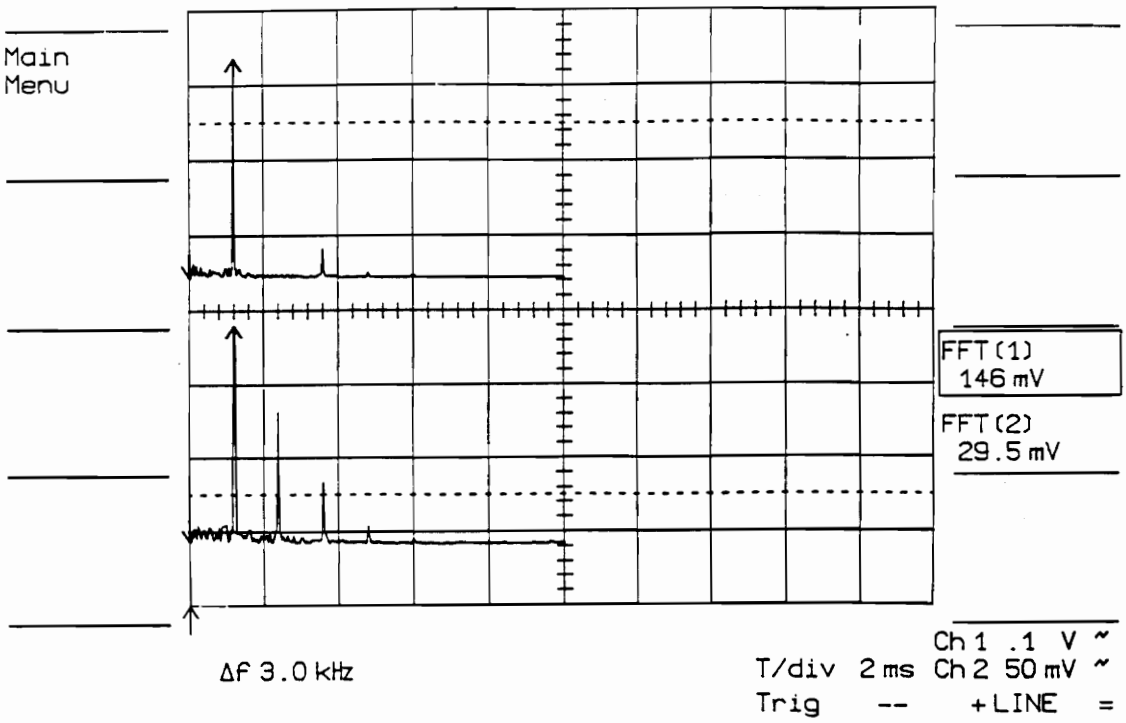

Figure 5.5 a) FFT of the output of a single EFPI at the sensor head (upper traces, at D1) and the SCEFI (lower traces, at D2), for a signal applied to the sensor head alone.

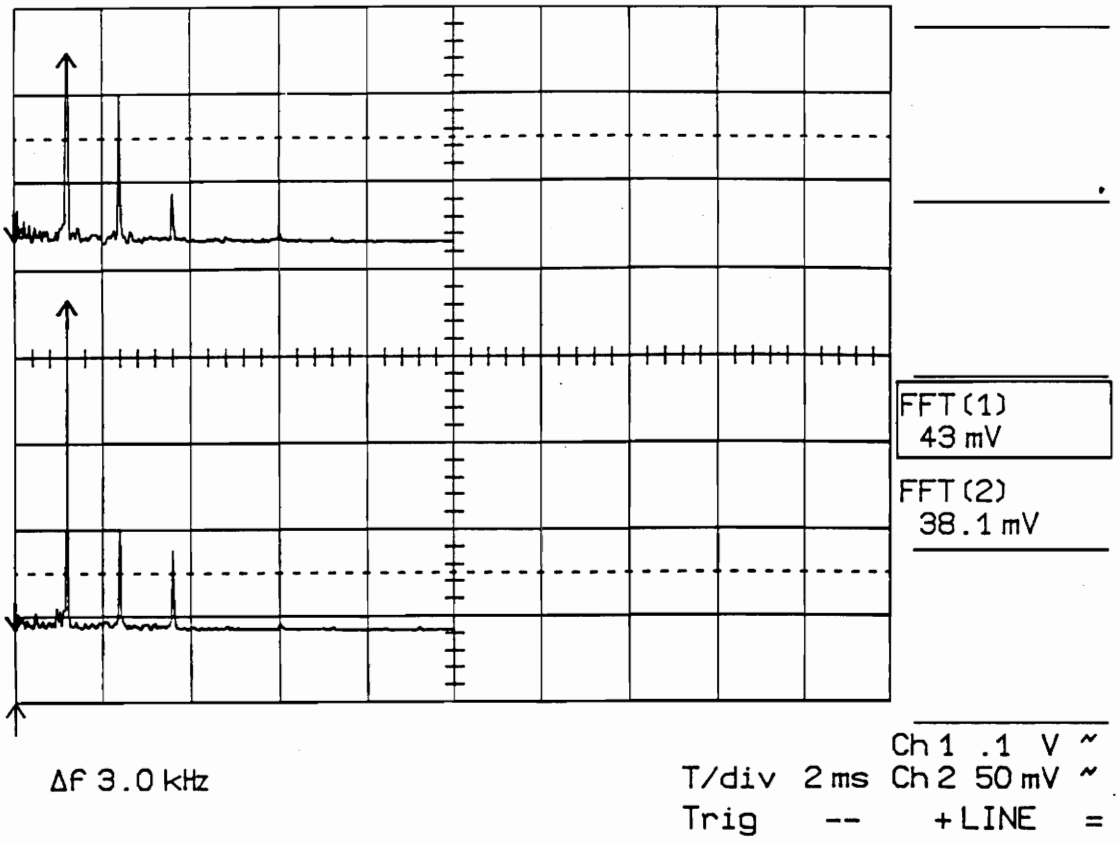

Figure 5.5 b) FFT of the output of a single EFPI at the sensor head (upper traces, at D1) and the SCEFI (lower traces, at D2), for a signal applied to the sensor head alone, for a different sampling instant.

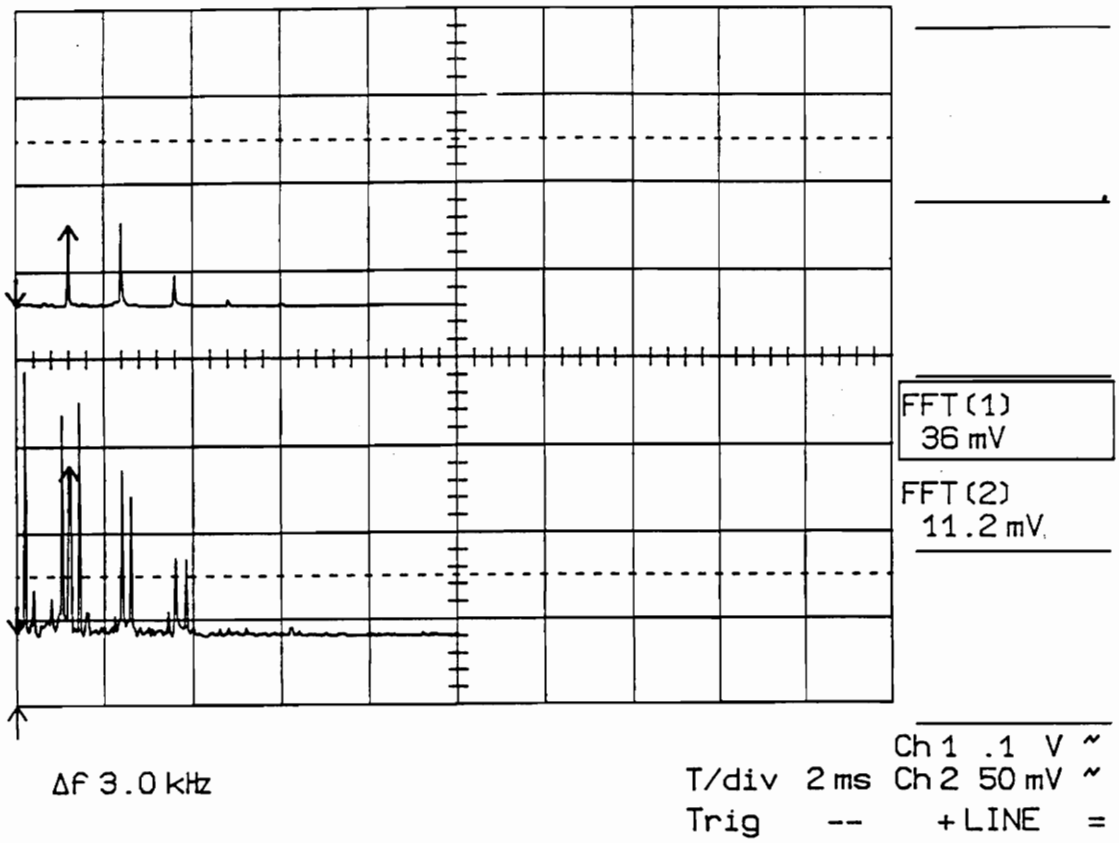

Figure 5.5 c) FFT of the output of a single EFPI at the sensor head (upper traces, at D1) and the SCEFI (lower traces, at D2), for a signal applied to both the sensor head and the modulator head.

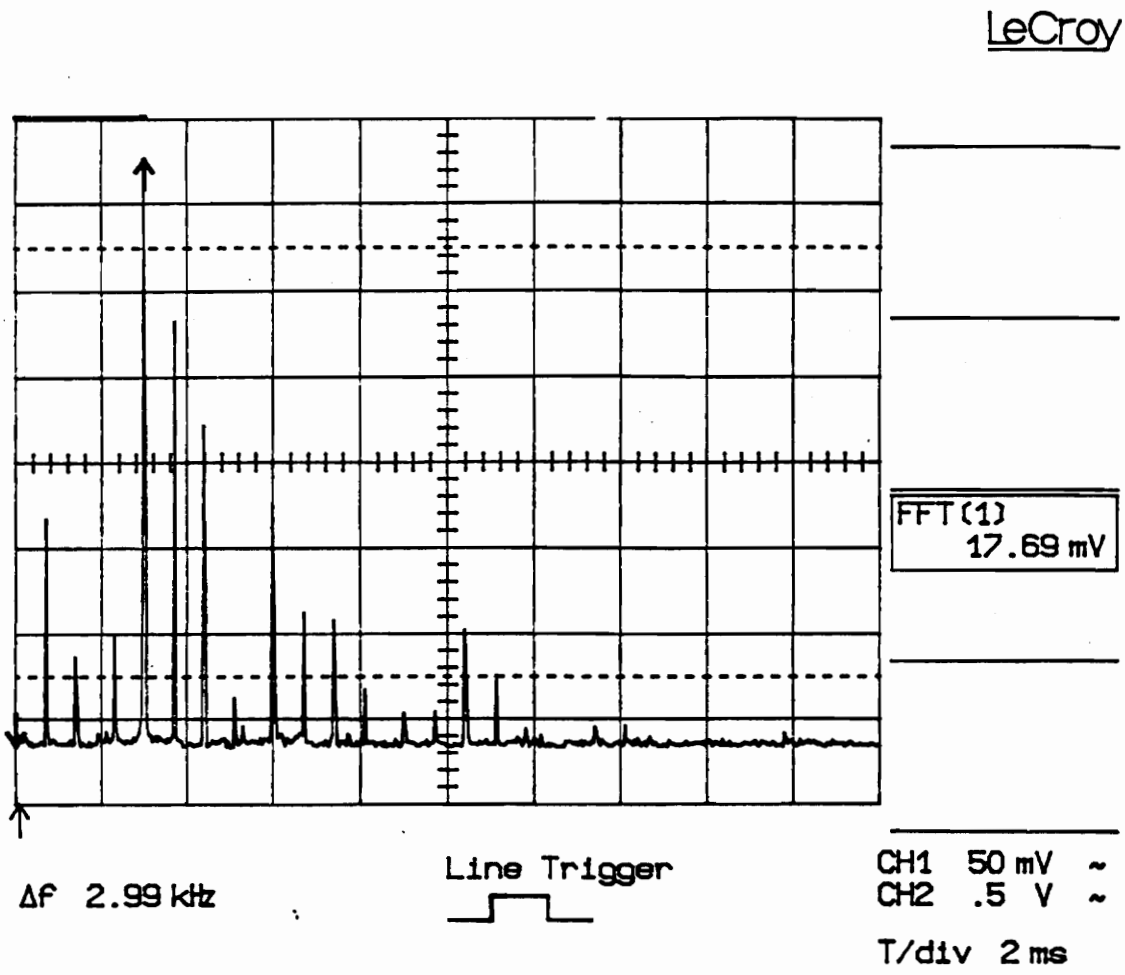

Figure 5.6 a) FFT of the SCEFI output at D4 for signal at 2.99 kHz and modulator at 3.69 kHz.

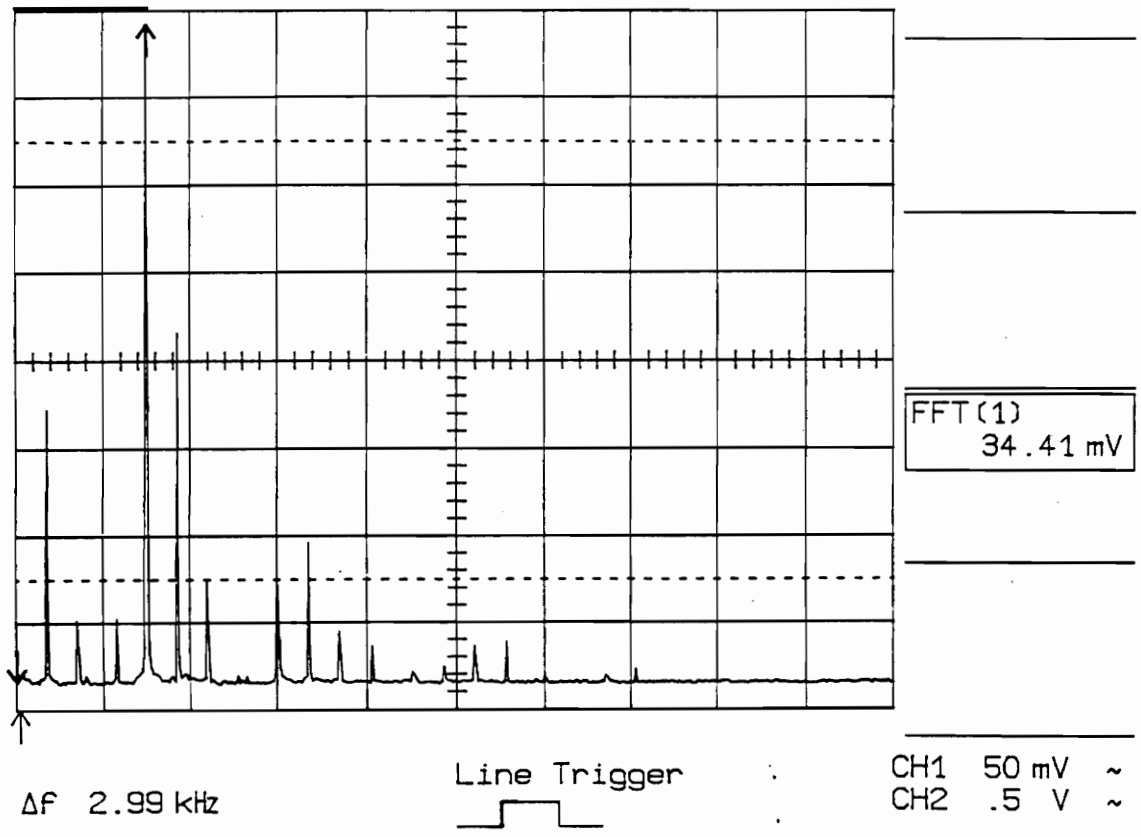

Figure 5.6 b) FFT of the SCEFI output at D4 for signal at 2.99 kHz and modulator at 3.69 kHz, for a different sampling instant.

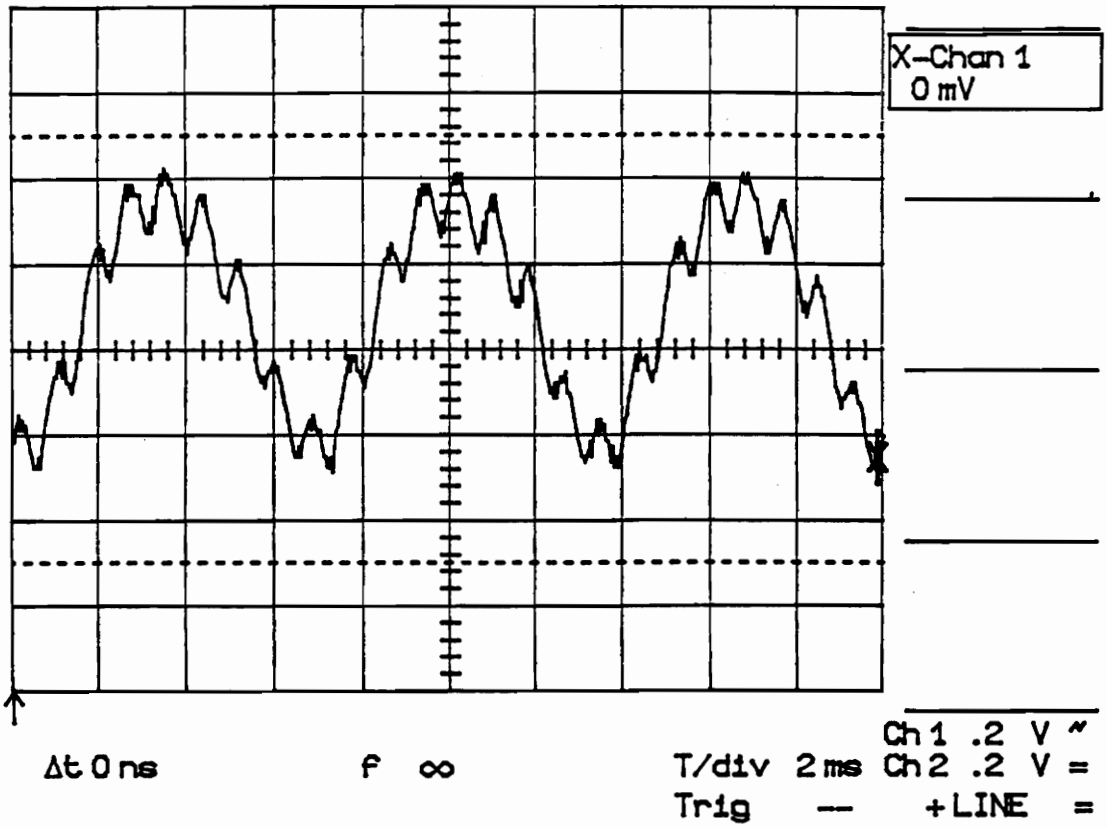

Figure 5.7 a) Time domain plot of the SCEFI output at D4 for an injection current of 28.2 mA.

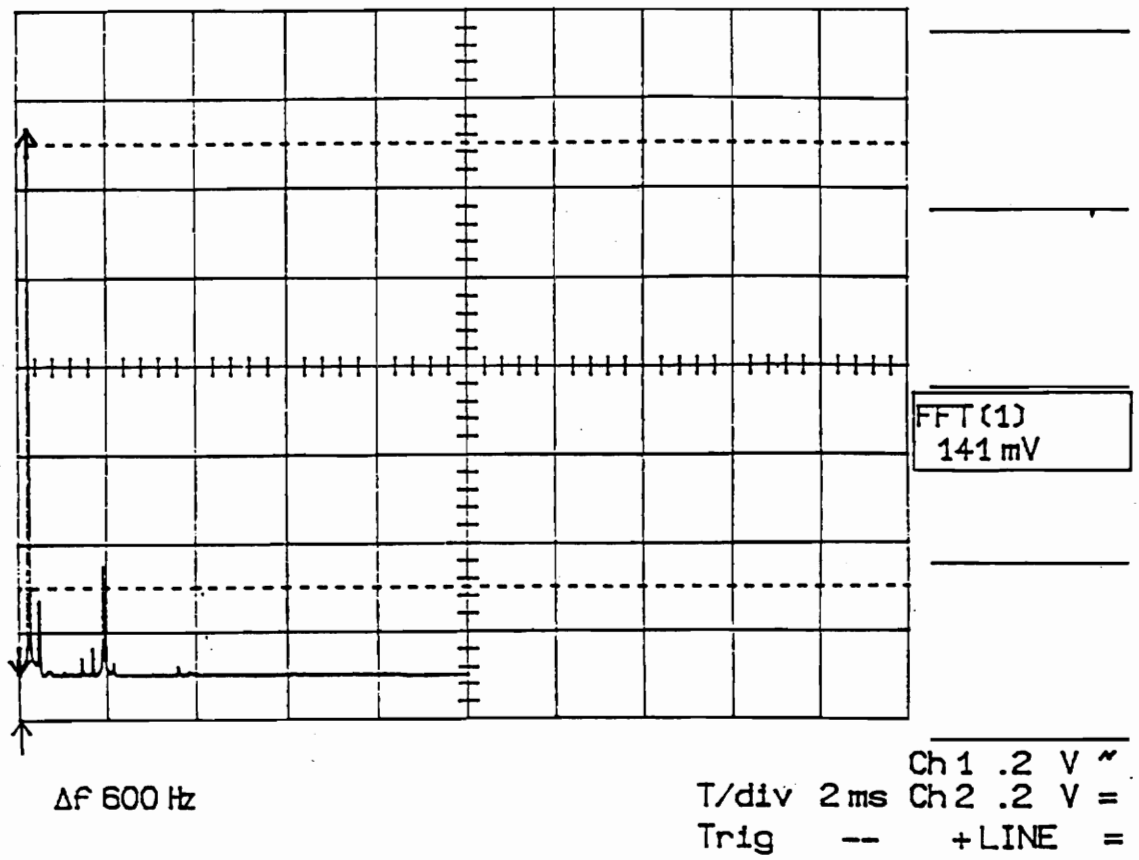

Figure 5.7 b) Frequency domain plot of the SCEFI output at D4 for an injection current of 28.2 mA.

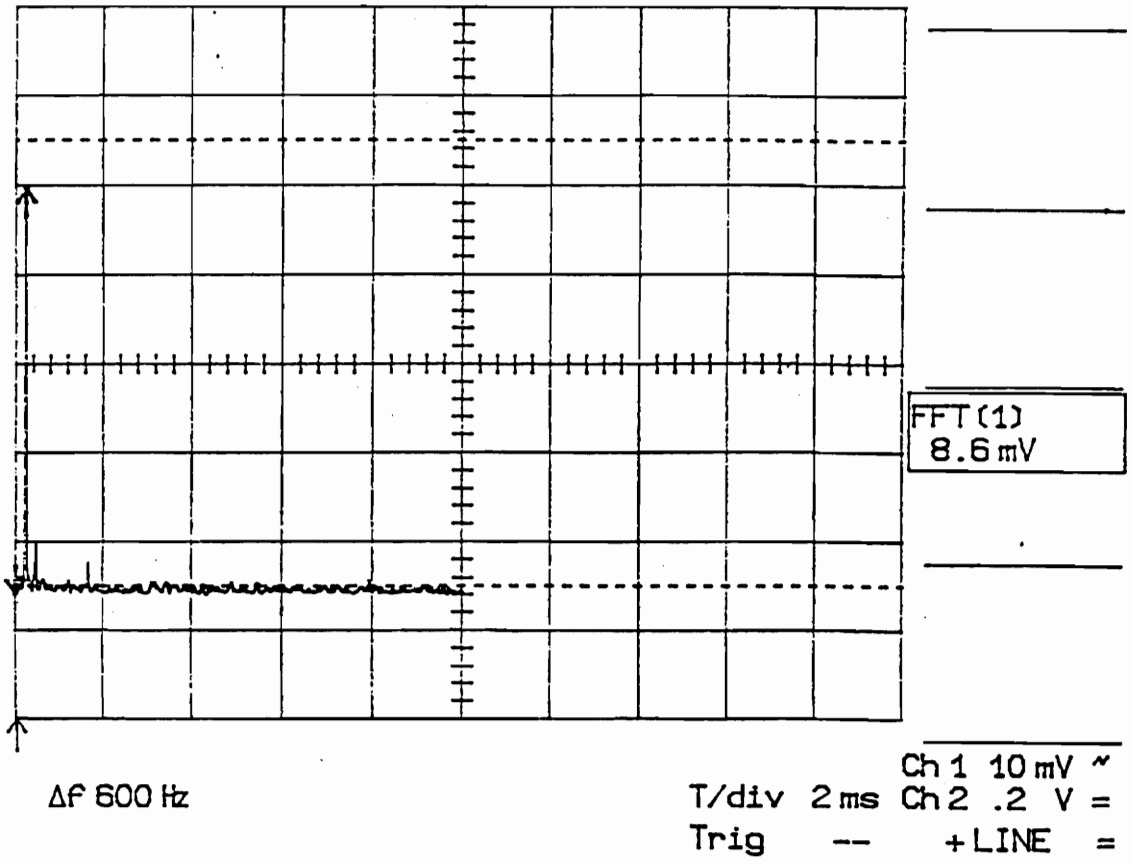

Figure 5.8 a) FFT of the SCEFI output at D4 for an injection current of 29.8 mA.

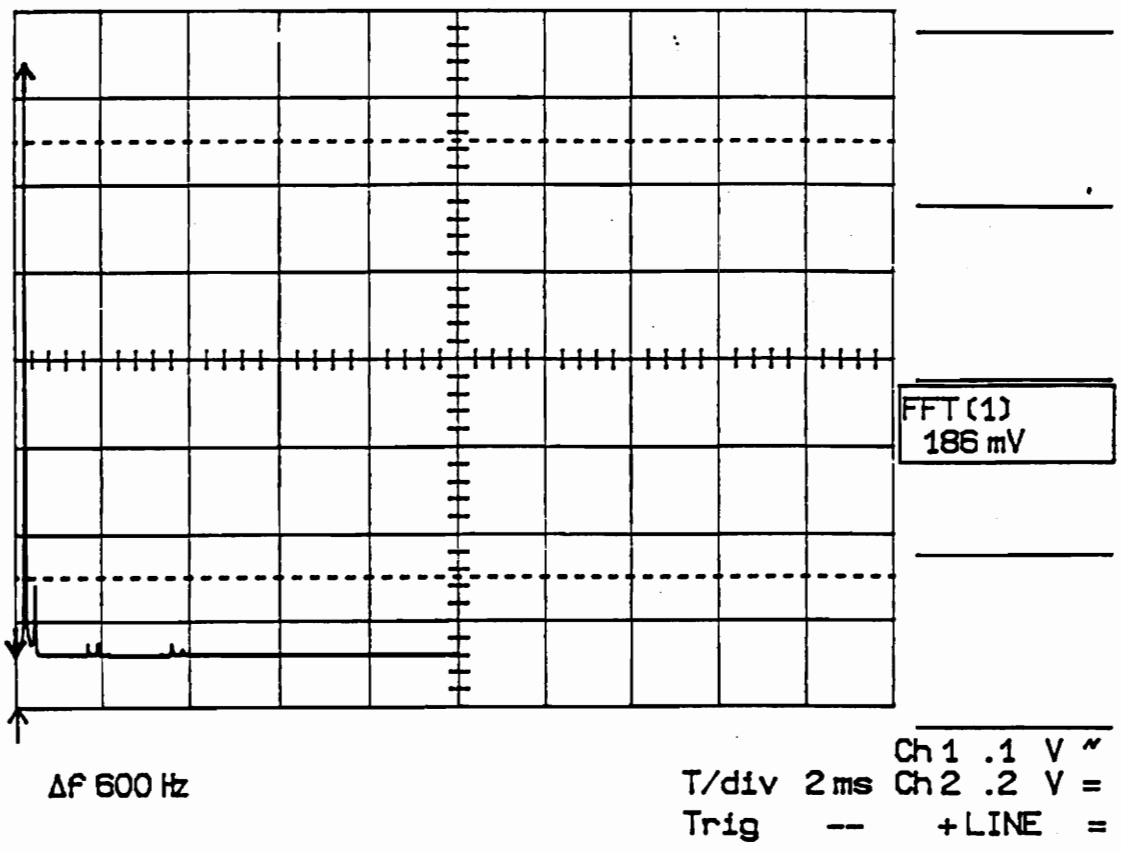

Figure 5.8 b) FFT of the SCEFI output at D4 for an injection current of 30.1 mA.

Chapter 6. Applications to two-sensor multiplexing

6.1 Introduction

An important requirement of fiber optic sensor systems is the capability to multiplex the signals to and from more than one sensor [22]. This involves a higher level of sophistication in the detection scheme devised for signal demodulation. Also, certain fiber interferometric sensor systems utilize broadband sources requiring two interferometers in tandem to demodulate the encoded phase signal. Thus a tandem sensor configuration assumes significance for generic fiber interferometric sensing.

The new configuration of the EFPI, called the Split-cavity Cross-coupled Extrinsic Fiber Interferometer (SCEFI), has the ability to multiplex two sensors, using a single laser source [22]. The SCEFI, described in Chapters 4 and 5 of this thesis, eliminates the need of biasing the EFPI at the quadrature point and thus, the effect of intensity variation with gap length change. The secondary phase modulation acts on the modulator head at the same side of the coupler as the source, while the signal acts on the EFPI sensor head

remote from the source. This split-cavity version has wide applications for fiber optic spectrometry and the control of the Fabry-Perot length.

6.2 Spectrum analysis detection method for multiplexing

In Chapter 4 of this thesis, a new spectrum analysis scheme for the SCEFI, based on the generic Bessel recurrence technique, was developed. The voltage amplitudes utilized in the detection scheme are given below as,

$$A = 4NPJ_1(2x)J_1(2y) \tag{6.1}$$

$$B = 4NQJ_1(2x)J_2(2y) \tag{6.2}$$

$$C = 4NPJ_2(2x)J_2(2y) \tag{6.3}$$

$$D = 4NQJ_2(2x)J_1(2y) \tag{6.4}$$

$$E = 4NJ_1(2x)\left[QJ_0(2y) + \sin(2\phi_s)\right] \tag{6.5}$$

$$F = 4NJ_3(2x)\left[QJ_0(2y) + \sin(2\phi_s)\right] \tag{6.6}$$

The values of A, B, C, D, E and F denote voltage amplitudes at different frequency components and are,

$A = V(|f_s \pm f_c|)$

$B = V(|f_s \pm 2f_c|)$

$C = V(2|(f_s \pm f_c)|)$

$D = V(|2f_s \pm f_c|)$

$E = V(f_s)$

$F = V(3f_s)$

In the above equations, $P = \cos(2(\phi_a + \phi_b))$ and $Q = \sin(2(\phi_a + \phi_b))$

The sensor phase shift 2x is given by,

$$2x = \frac{4\sqrt{(C\,D)}}{\sqrt{A\,B}\left[1 + \frac{F}{E}\right]} \tag{6.7}$$

We call this measurement of 2x for the SCEFI as the J_1-J_3 method.

Secondary phase modulation in the EFPI is now possible with the SCEFI and leads to two sensor multiplexing [22] by concurrent measurement of 2y.

Consider the frequency components at $3f_c$ and f_c. Let the amplitudes at these components be given by I and K. Thus $I = V(3f_c)$ and $K = V(f_c)$.

From equation 4.2, the term $\cos 2(\phi_c + \phi_b)$ can be written as,

$$\cos 2(\phi_c + \phi_b) = \cos 2\,(y \sin \omega_c t + \phi_b)$$

$$= \cos(2y \sin\omega_c t)\cos(2\phi_b) - \sin(2y \sin\omega_c t)\sin(2\phi_b)$$

$$= \left[J_0(2y) + 2J_2(2y)\cos(2\omega_2 t)\right]\cos(2\phi_b) - \left[2J_1(2y)\sin(\omega_2 t) + 2J_3(2y)\sin(3\omega_2 t)\right]\sin(2\phi_b) \quad (6.8)$$

From equation 4.6 and 6.8, we can write expressions for **I** and **K**.

The components corresponding to $I = V(3f_c)$ are:

$$2J_3(2y)\sin(3\omega_c t)\sin(2\phi_b) + 2J_0(2x)J_3(2y)\sin 2\phi \sin(3\omega_c t)$$

Thus,

$$\mathbf{I = 4NJ_3(2y)\left[QJ_0(2x) + \sin(2\phi_b)\right]} \quad \mathbf{(6.9)}$$

The components corresponding to $K = V(f_c)$ are:

$$2J_1(2y)\sin(\omega_c t)\sin(2\phi_b) + 2J_0(2x)J_1(2y)\sin 2\phi \sin(\omega_c t)$$

Thus,

$$\mathbf{K = 4NJ_1(2y)\left[QJ_0(2x) + \sin(2\phi_b)\right]} \quad \mathbf{(6.10)}$$

Therefore the expression for the phase shift 2y of the second sensor is given by [22],

$$2y = \frac{4\sqrt{(CB)}}{\sqrt{AD}\left[1 + \frac{I}{K}\right]} \qquad (6.11)$$

6.3 Experimental arrangement

A fused directional coupler with a splitting ratio of 50:50 was used to split the light from a laser diode operating at 1300 nm. No optical isolator was used though it would be desirable to reduce end-reflection interference effects on both the source and the SCEFI transfer function. The schematic of the SCEFI and the test modulator arrangement is shown in Figure 6.1. The two ends of the EFPI were attached to a thin piezoelectric PZT (lead-zirconate-titanate) plate with an epoxy. Bonding the whole length of the EFPI on the PZT plate would eliminate the variations in the induced phase shift as a function of time. However, such a bonding condition also reduces the phase shift that can be derived from the PZT because of mechanical loading.

The output signal from the interferometer was extremely sensitive to the number of modes supported by the laser cavity. The number of modes supported varies from a single mode with large power at certain periodic injection current levels on to more than ten modes that could be supported at other current levels. The optical power spectrum of the laser diode recorded for two different arbitrary injection current levels is shown in Figure 6.2 [22]. This figure shows the power in a single, strong mode in Figure 6.2b, is distributed among several modes in Figure 6.2a. The laser diode was therefore operated only at current levels corresponding to Figure 6.2b.

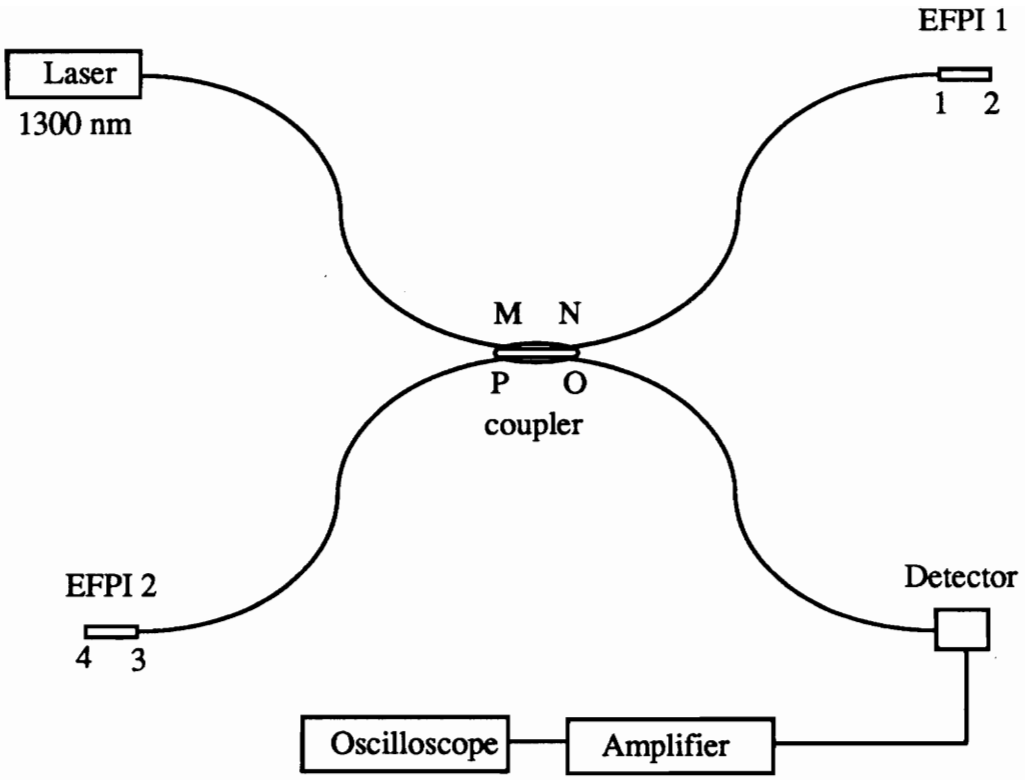

Figure 6.1 a) Schematic of the SCEFI.

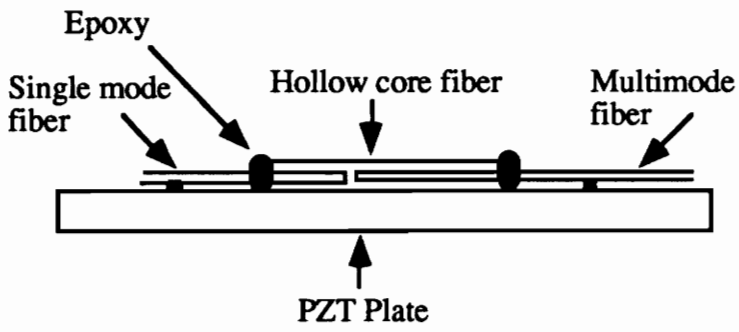

Figure 6.1 b) Test modulator arrangement for each sensor head.

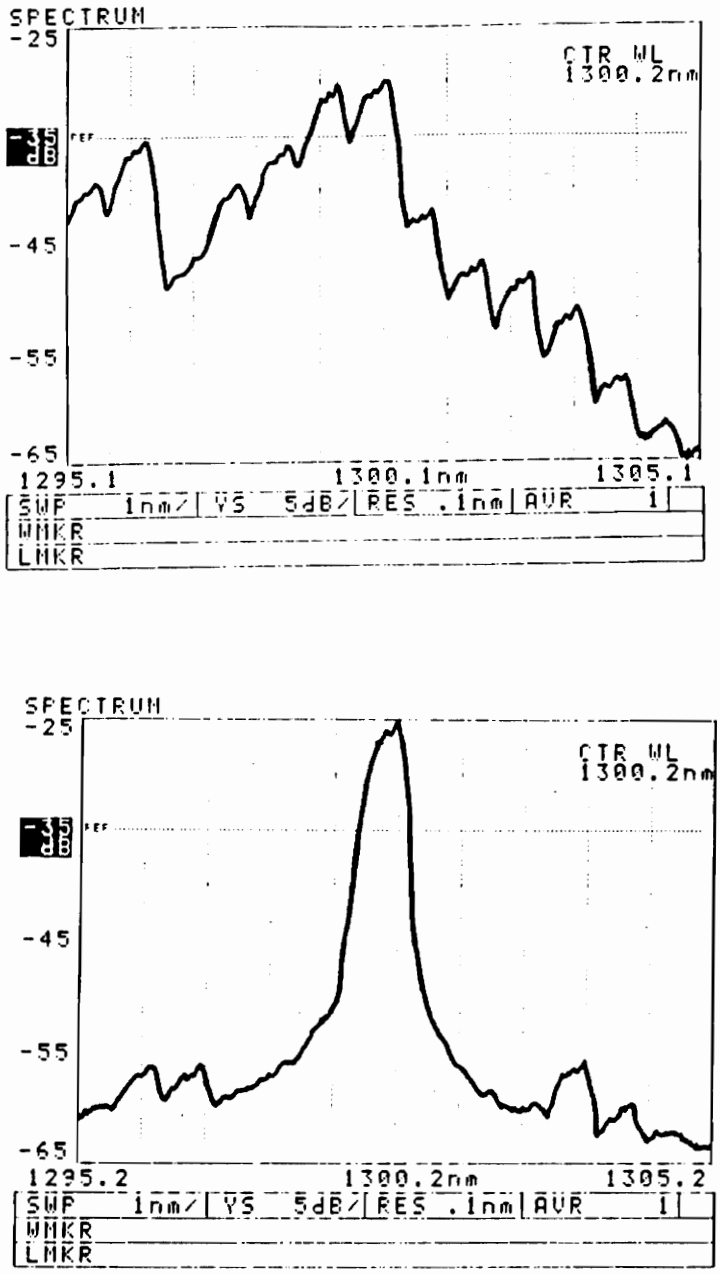

Figure 6.2 Optical spectrum of the laser diode output.

a) several modes b) single strong mode

6.4 Results and discussion

Figure 6.3 [22] shows the FFT of the photovoltage output for an input of 45 V at 1.4 kHz to the EFPI 1. The EFPI 2 was not driven by any signal for this plot. It should be noted that though a single EFPI was driven, the signal seen at the detector traverses both the EFPI's. The voltage amplitudes seen at the multiples of the fundamental frequency of 1.4 kHz were utilized through the $J_1..J_4$ method to calculate the dynamic phase shift. For the input voltage of 45 V for the EFPI 1, the phase shift from Figure 6.3 was measured to be 1.28 rad.

Figure 6.4 [22] shows the FFT of the SCEFI output for an input voltage of 25 V to each of the two EFPI's. The simultaneous measurement of the phase shift for the two EFPI's through the use of equations 6.7 and 6.11 provided 0.818 rad for the EFPI 1 and 0.791 rad for the EFPI 2. The difference in the values of the phase shift was as expected because it is difficult to exactly match the bonding conditions for the two test modulators. Figure 6.5 [22] shows the frequency domain output (upper trace) and the time domain output (lower trace) for the SCEFI for an input voltage of 34 V to both the EFPI's. The utilizations of the equations 6.7 and 6.11 provided 0.99 rad and 0.96 rad for the two EFPI's. The good agreement seen in the phase measurements for the plots in Figures 6.5 and 6.6 establishes the validity of the expressions used here for the simultaneous and yet independent measurement of the phase shift signals from the two EFPI's.

The multiplexing of the two EFPI's on a single coupler demonstrated with the SCEFI configuration is brought out in Figure 6.6 [22] wherein the phase shift measured by the $J_1.J_3$ method of equations 6.7 and 6.11 for the two EFPI's is plotted as a function of the input voltage applied to the PZT test modulators.

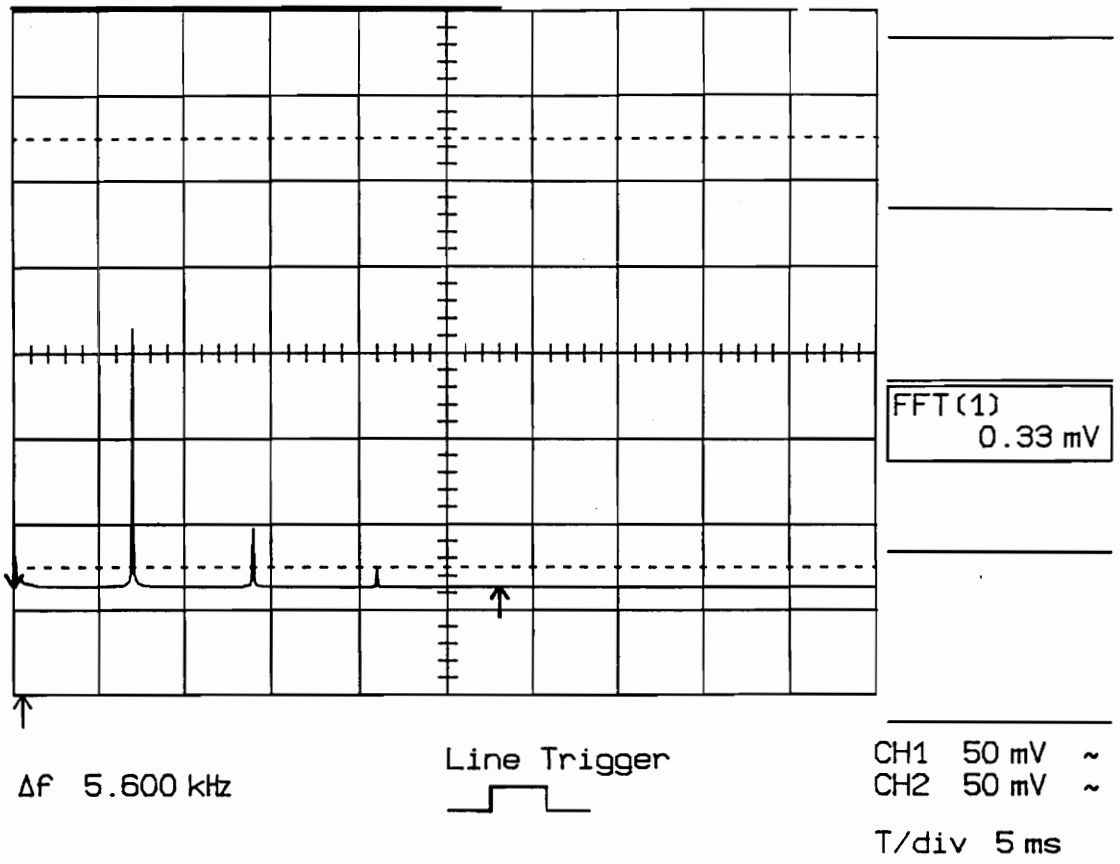

Figure 6.3 FFT of the detector output for an input of 45 V at 1.4 kHz to EFPI 1, with no drive to EFPI 2.

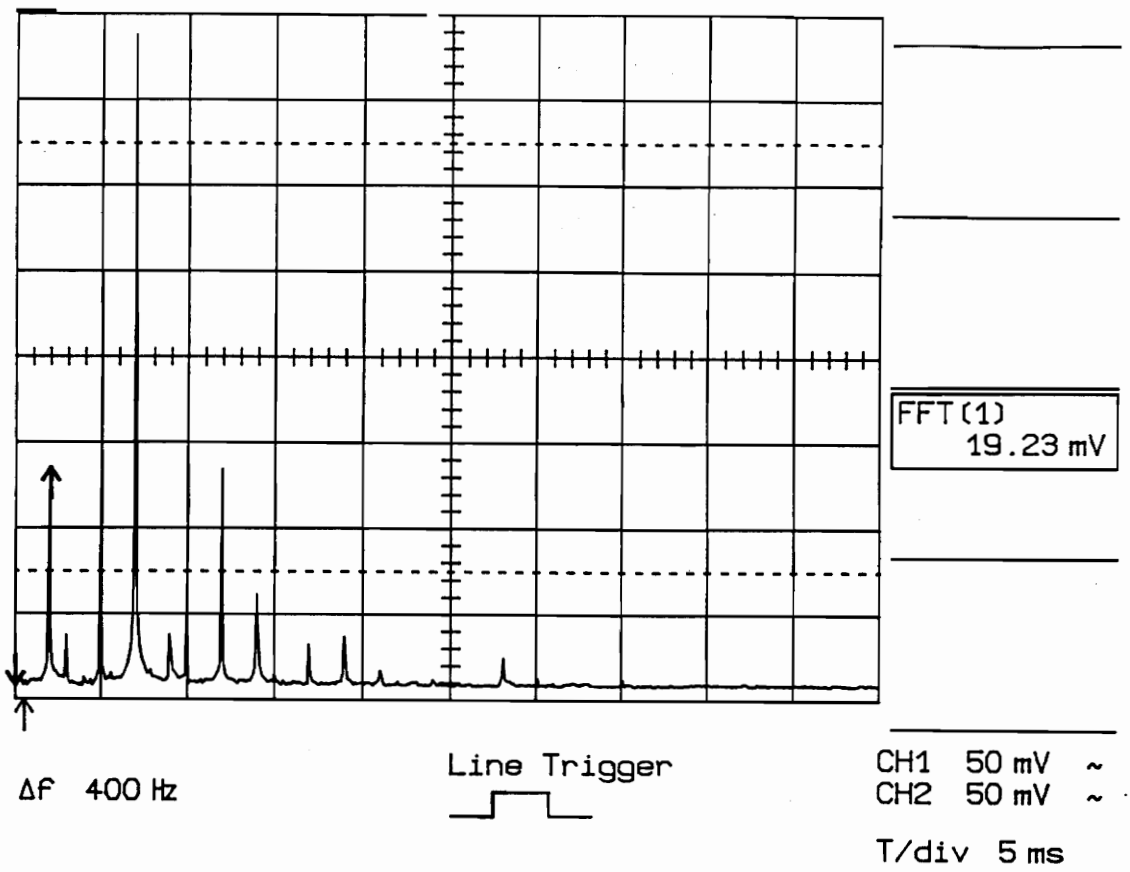

Figure 6.4 FFT of the SCEFI output for an input voltage of 25 V to each of the two EFPI's.

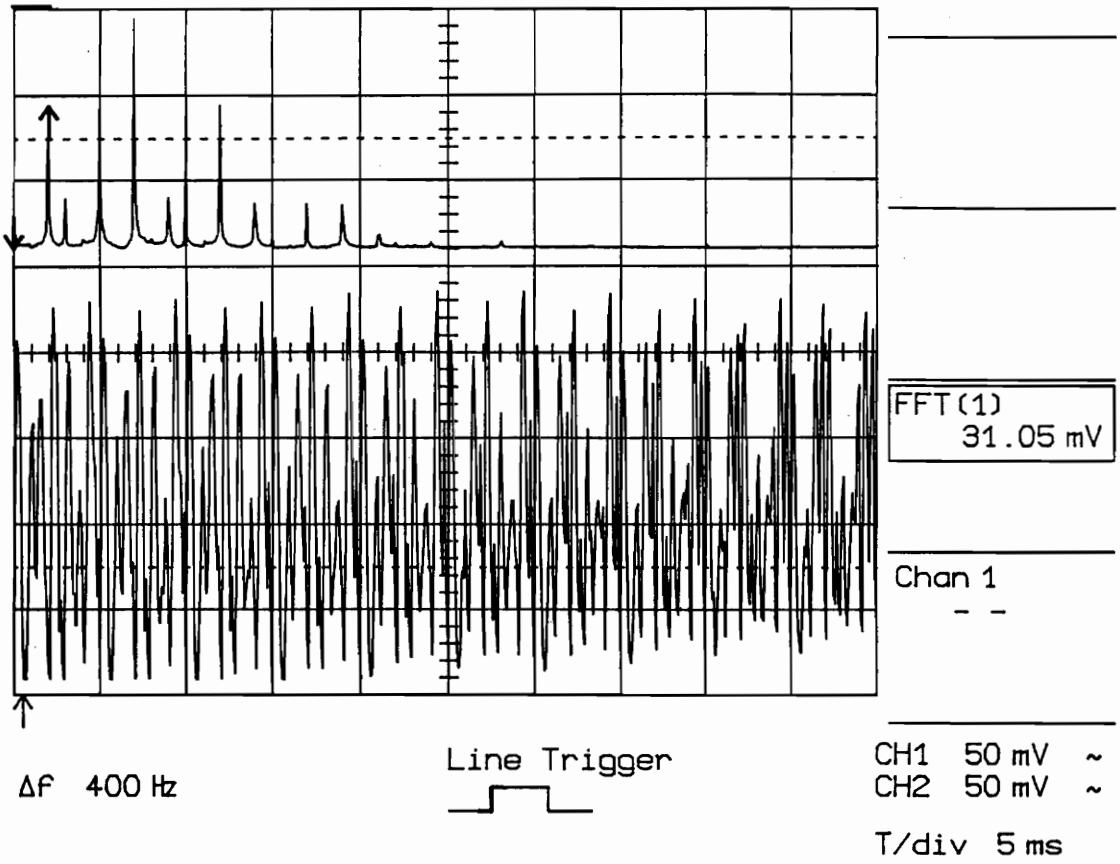

Figure 6.5 Frequency domain and time domain outputs for the SCEFI for an input voltage of 34 V to both the EFPI's.

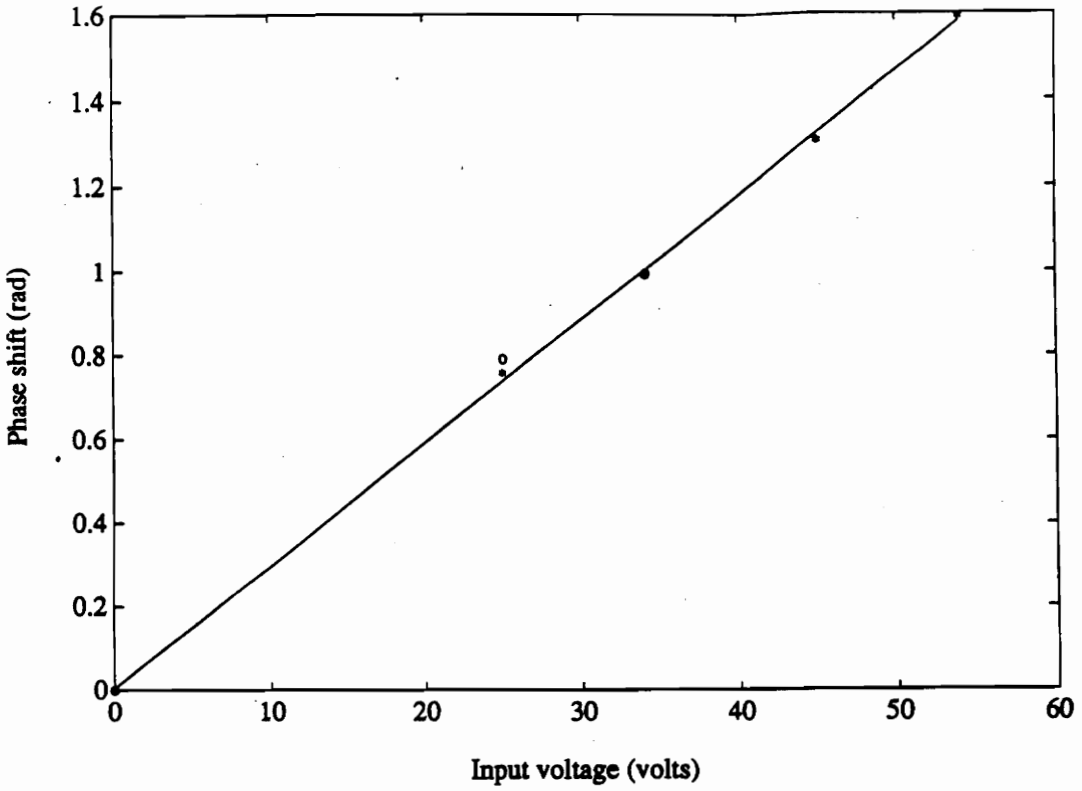

Figure 6.6 Phase shift measured by $J_1.J_3$ method as a function of input voltage to the PZT test modulators.

Chapter 7. Conclusions and Future Directions

7.1 Conclusions

In this thesis, a new configuration of the Extrinsic Fabry-Perot Interferometer (EFPI) has been demonstrated. The EFPI is very suitable for fiber sensor applications, especially in the area of smart materials. It's small size and geometry make it an ideal candidate for such applications. The Split-cavity Cross-coupled Extrinsic Fiber Interferometer (SCEFI), developed and demonstrated in this thesis, is a versatile configuration of the EFPI. It overcomes the limitations imposed by real field conditions. The new spectrum analysis scheme developed for the SCEFI, provides a linear phase shift readout. The spectrum analysis scheme also overcomes the problems of signal fading due to random drifts, variations in the fringe visibility of the sensor and intensity variations in the source. The theoretical model of four-beam interference has been validated through the experiments performed on this new configuration. The SCEFI also allows the introduction of secondary phase modulation in the EFPI. The additional drift introduced in the modulator head provides possibilities for remote sensor stabilization.

In addition, the applicability of this sensor configuration to two sensor multiplexing, using a single laser source and a single coupler, has been demonstrated. This multiplexed version of the EFPI provides simultaneous and independent readouts of the phase shifts in the two sensors.

7.2 Future directions

An important next step in the development of the SCEFI would be in the stabilization of the sensor head, using feedback techniques, to the modulator head. This will result in the stabilization of the SCEFI output. One of the references [25] provides a pointer in this direction.

Another aspect to be examined would be the bonding techniques of the EFPI sensor heads to the piezoelectric elements. This would result in the values of the measured phase shifts to having smaller standard deviation, than those currently obtained.

The new, versatile configuration of the EFPI, demonstrated in this thesis, has a number of applications in fiber optic sensing and instrumentation systems. These include:
(a) static phase measurements in addition to dynamic signals. This can be done by superimposing very small static phase shifts on a dynamic modulation at the modulator EFPI. A recent spectrum analysis scheme [26] based on a $\tan^{-1}$ algorithm allows dc phase shift measurements to a high accuracy. This, with suitable modification to take into account the interference terms, would facilitate measurement of quasi-static signals.
(b) use of the FMCW scheme [27], based on linear source-frequency modulation, by replacing the modulator EFPI head with a long fiber terminated in reflective ends. This

will result in an appreciably high carrier beat frequency on which the relatively small signal frequency deviation would appear as sidebands.

(c) three sensor frequency division multiplexing and its subsequent extension to three-sensor strain rosettes, possible with the use of a 3x3 directional coupler.

Apart from sensor applications, the action of the SCEFI as a split cavity filter for WDM systems presents new possibilities for remote compensation of the Fabry-Perot etalon.

References

[1] T. G. Giallorenzi, J. A. Bucaro, A. Dandridge, G.H. Sigel, JR., J. H. Cole, S. C. Rashleigh, and R. G. Priest, "Optical Fiber Sensor Technology," *IEEE Journal of Quantum Electronics,* vol. QE-18, no. 4, pp. 626-664, April 1982.

[2] E. Udd, *Fiber Optic Sensors: An Introduction for Engineers and Scientists*, New York, John Wiley and Sons, 1991.

[3] A. Wang, M. S. Miller, M. F. Gunther, K. A. Murphy, and R. O. Claus, "Loss-compensation technique using a split-spectrum approach for optical fiber air-gap intensity-based strain gages," *SEM Conference*, Michigan, June 1993.

[4] A. Dandridge, A.B. Tveten and T.G. Giallorenzi, "Homodyne Demodulation Scheme for Fiber Optic Sensors using the Phase Generated Carrier," *IEEE Journal of Quantum Electronics*, vol. QE-18, no. 10, pp. 1647-1653, 1987.

[5] T. Yoshimo, K. Kurosawa, K. Itoh, and T. Ore, "Fiber-optic Fabry-Perot interferometer and its sensor applications," *IEEE Journal of Quantum Electronics*, vol. QE-18, no. 10, pp. 1624, 1982.

[6] K. A. Murphy, M. F. Gunther, A. M. Vengsarkar, and R. O. Claus, "Quadrature phase-shifted, extrinsic Fabry-Perot Optical fiber sensors," *Optics Letters,* vol. 16, no. 4, pp. 273-275, February 1991.

[7] E. Hecht, *"Optics"*, Second edition, pp 366, Addison-Wesley Publishing Co., Massachusetts, 1987.

[8] V. S. Sudarshanam, R. R. Dhawan, and R. O. Claus, "The split-cavity cross-coupled extrinsic fiber interferometer," *Proc. SPIE Conf. fiber optic smart structures and skins V*, Boston, 1992.

[9] D.A. Jackson, "Monomode optical fiber interferometers for precision measurement," *Instrument Science and Technology*, pp. 980-1001, 1985.

[10] Yoshihiro Ohtsuka, "Dynamic measurements of small displacements by laser interferometry,"*Trans Inst M C* , Vol. 4, No. 3, pp. 115-124, July-Sept 1982.

[11] V.S. Sudarshanam and K. Srinivasan, "Linear readout of dynamic phase change in a fiber-optic homodyne interferometer," *Optics Letters* , vol. 14, no. 2, 1989.

[12] T. Yoshino, K. Kurosawa, K.Itoh, and T. Ose, "Fiber optic Fabry-Perot interferometer and its sensor applications," *IEEE Journal of Quantum Electronics*, QE-18, 1624, 1982.

[13] S.J. Petuchowski, T.G. Giallorenzi, and S.K. Sheem, "A sensitive fiber optic Fabry Perot interferometer," *IEEE Journal of Quantum Electronics*, QE-17, 2168, 1981.

[14] A.D. Kersey, D.A. Jackson, and M. Corke, "A simple Fabry Perot sensor," *Optic Communications*, 45 , pp. 71, 1983.

[15] S. R. Mallison, "Wavelength-selective filters for single mode fiber WDM systems using Fabry Perot interferometers," *Applied Optics*, 26, pp. 430, 1987.

[16] R. O. Claus, Ed., *Proceedings Conference on optical fiber sensor-based smart materials and structures*, Institute of Physics Publishing Inc., Philadelphia, 1992.

[17] D. W. Stowe, W. E. Moore, and V. J. Tekippe, "Passive quadrature demodulation for interferometric sensors," *Proceedings of SPIE Fiber optic and laser sensors*, pp. 148, 1983.

[18] V. S. Sudarshanam, "Minimum detectable phase shift in spectrum analysis techniques of optical interferometric vibration detection," *Applied Optics*, 31 ,1992.

[19] V. S. Sudarshanam, "New spectrum analysis technique for interferometric vibration detection," *Optic Communications*, 88, pp. 291, 1992.

[20] A. Dandridge, A.B. Tveten, and T.G. Giallorenzi, "Homodyne demodulation scheme for fiber optic sensors using phase modulated carrier," *IEEE Transaction on Microwave Theory and Techniques*, MTT-30, pp. 1635, 1982.

[21] V. S. Sudarshanam, R. R. Dhawan, and R. O. Claus, "Extrinsic fiber-optic interferometer with a cross-coupled split cavity," *OFC/IOOC '93 Technical Digest*, pp. 139-140, 1993.

[22] V. S. Sudarshanam, R. R. Dhawan, T. Tran, M. K. Burford, and R. O. Claus, "Two sensor multiplexing in a split cavity cross coupled extrinsic fiber interferometer," *Proc. SPIE*, Albuquerque, New Mexico, February 1993.

[23] V. S. Sudarshanam and R. O. Claus, "Split-cavity cross-coupled extrinsic fiber-optic interferometric sensor," *Optics Letters*, vol. 18, no. 7, pp. 1-3, April 1993.

[24] V. S. Sudarshanam, "Linear measurement of static phase change in optical homodyne interferometers: an analysis," *Optics Letters*, 17, pp 682, 1992.

[25] K. Fritsch and G. Adamovsky, "Simple circuit for feedback stabilization of a single mode optical fiber interferometer," *Rev. Sci. Instrum.*, 52(7), pp. 996-1000, July 1981.

[26] P. Urquhart, "Transversely coupled fiber Fabry Perot resonator theory," *Applied Optics*, 26, pp. 456, 1987.

[27] D. Uttam, and B. Culshaw, "Precision time domain reflectometry in optical fiber systems using a frequency modulated continuous wave ranging technique," *Journal of Lightwave Technology*, LT-3, pp. 971, 1985.

Vita

Rajat R. Dhawan was born in Calcutta, India, on December 8, 1967. In 1985, he finished his Higher Secondary Certificate examination from K. C. College, Bombay and was accepted into the Electronics Engineering program of University of Bombay. After completing his Bachelor of Engineering in 1989, he enrolled in the Master of Science program in the Bradley Department of Electrical Engineering at Virginia Polytechnic Institute and State University, Blacksburg. During his stay at Virginia Tech, Mr. Dhawan was employed at the Fiber and Electro-optics Research Center as a Graduate Research Assistant with research interests in fiber optic sensors, devices and systems. He received his Master's degree in August 1994.

His professional interests include optical fiber systems, communication technology and computer hardware design. He is a member of the Institute of Electrical and Electronics Engineers.